Received: 10 October 2023 | Revised: 26 September 2024 | Accepted: 15 October 2024
DOI: 10.1002/suco.202300875

ARTICLE

Hyperbolic/elliptic-CAP formulation for FRCC based on microplane constitutive theory

Antonio Caggiano[1] | **Sonia M. Vrech**[2,3] | **Guillermo Etse**[3,4]

[1]DICCA, Department of Civil, Chemical and Environmental Engineering, University of Genova, Genoa, Italy
[2]CONICET, National Scientific and Technical Research Council, Buenos Aires, Argentina
[3]CEMNCI, Center for Numerical and Computational Methods in Engineering, Faculty of Exact Sciences and Engineering, National University of Tucuman, Tucumán, Argentina
[4]LMNI, Laboratory of Numerical Methods in Engineering, Universidad de Buenos Aires, Buenos Aires, Argentina

Correspondence
Antonio Caggiano, DICCA, Department of Civil, Chemical and Environmental Engineering, University of Genova, Via Montallegro 1, Genova 16145, Italy.
Email: antonio.caggiano@unige.it

Abstract
The present work describes an elasto-plastic constitutive formulation aimed at simulating the failure behavior of Fiber Reinforced Cementitious Composites (FRCCs). This proposal, based on the Microplane Theory and Smeared Crack Approach (SCA), assumes a hyperbolic maximum strength criterion for the cementitious matrix in terms of normal and shear (micro-)stresses, evaluated on generally oriented planes (microplanes). A combination of an associated/non-associated plastic flow rule in conjunction with a fracture energy-based softening law is defined to complete the modeling approach. The Mixture Theory is applied with the aim of characterizing the fiber-to-concrete interactions, described by considering two fundamental interaction phenomena: bridging debonding effects and dowel actions. Numerical analysis of FRCC failure behavior at the constitutive level is performed. Particularly, the soundness and capabilities of this approach are assessed against experimental data from tensile, shear, and compressive tests on FRCC samples. Simple shear tests are also evaluated to analyze the influence of the microplanes approximation over the unit microplane hemisphere. Comparisons against a discontinuous zero-thickness interface model are proposed. Numerical results also illustrate the capabilities of the proposed constitutive theory to reproduce brittle or localized failure modes in limit stress states through discontinuous bifurcation analysis.

KEYWORDS
concrete, failure, fibers, FRCC, microplanes, mixture theory

1 | INTRODUCTION

Fiber-Reinforced Cementitious Composites (FRCCs) encompass a large class of materials whose properties are strongly dependent on the successful matching between the matrix and the reinforcing phase.[1] In particular, mixing short randomly dispersed fibers (e.g., made of glass,[2] steel,[3,4] polypropylene,[5,6] etc.) in a cementitious matrix is a well-established technique currently widespread in the construction sector.[7,8] Even printed fibers have been used as reinforcements for cementitious matrices.[9] A clear example of this type of materials is represented by the Steel Fiber Reinforced Concrete (SFRC) whose greatest advantage, compared with plain concretes, is its higher residual tensile strength accompanied with elevated toughness in post-cracking regime.[10,11] Regarding both tensile and/or bending behavior, a strain-hardening response with multiple cracks and large energy

This is an open access article under the terms of the Creative Commons Attribution License, which permits use, distribution and reproduction in any medium, provided the original work is properly cited.
© 2024 The Author(s). *Structural Concrete* published by John Wiley & Sons Ltd on behalf of International Federation for Structural Concrete.

absorption prior the failure can be achieved.[12] Whereas fiber bridging mechanisms mainly take place under cracked regime of concrete matrix, the mechanical behavior of uncracked members is practically not influenced by the addition of fibers beyond the limited increase of the elastic stiffness.

With the aim to describe and predict FRCC cracking onset and propagation, traditionally continuous and discrete constitutive theories have been successfully developed in the last decades. Discrete Crack Approaches (DCAs), incorporating strains and/or displacement jumps/discontinuities, describes cracks and the related evolution mechanisms in a more reliable way. The kinematic of cracking is modeled by means of the displacement field in discontinuities or interfaces in the Finite Element (FE) discretization.[13–15] Their main disadvantage reside on the low feasibility to be included in commercial FE codes.

On the other hand, SCA in which the failure and cracked zone is considered to be distributed along a certain region of the solid, is characterized by strong FE-mesh size dependence of the localization band width (e.g., a finer discretization leads to a decreasing toughness of the analyzed numerical model) and loss of ellipticity of the constitutive differential equations,[16] which requires the use of "ad-hoc" regularization procedures.[17–19] Nevertheless, the main advantages of employing SCA are due to their lower computational cost and the easier to be implemented in classical commercial or open-source codes.

Although SCA consists of a macroscopic approximation, it can be enriched by incorporating microscale participation by the Microplane Theory, originally proposed by Bažant and Oh.[20] It consists in the formulation of constitutive laws at microplane level defining the mechanical behavior of certain planes (the microplanes) generically orientated. Then, the macroscopic response shall be achieved through the consideration of appropriated thermodynamically consistent homogenization process over the responses in all microplanes.[21,22] Regarding cementitiuos materials, microplane-based constitutive models have been approached by Huang et al.,[23] Indriyantho et al.,[24] Kong et al.[25] a. o., whereas elasto-plastic microplane formulation for fiber reinforced concrete have been developed by Ferhun et al.,[26] Vrech et al.,[27] Xue and Kirane.[28]

In this framework, a novel elasto-plastic fracture energy-based microplane model for simulating the failure behavior of FRCC is formulated at material level. Thus, the advantage of its easy computational implementation and the achieved enrichment through the microscale information are combined. The constitutive formulation at the microplane level is described by a hyperbolic maximum strength criterion with an elliptical CAP surface for the cementitious matrix, relating micro-strains evaluated on generally orientated planes (microplanes). A plastic flow rule, combining associated and non-associated sections, in conjunction with a fracture energy-based softening law are adopted. Fiber effects on the composite failure behavior are taken into account through both a bond–slip formulation and a dowel model. The Mixture Theory accounts for the compound behavior, following the original approach proposed by Truesdell and Toupin[29] and further applied for concrete analysis by Ortiz and Popov,[30] Oller et al.,[31] Rastellini et al.,[32] and among others.

The analysis of the failure modes predicted by the material theories (localized or diffuse) is also addressed. Particularly important is the evaluation of brittle or localized failure modes that in the framework of continuous models are described by means of discontinuous bifurcations or jumps in the velocity gradients.

After this introductory section, the general basis of the proposed Microplane Theory are described in Section 2. Section 3 is related to the application of the well-known Mixture Theory to describe the mechanical behavior of FRCC, following previous contributions by Oliver et al.[33] and Vrech et al.[34] Particularly, Section 3.1 reports the constitutive laws proposed at microplane level featuring the hyperbolic maximum strength criterion with the elliptical CAP surface, the plastic flow rules and the fracture energy-based softening formulation for plain concrete. The fiber-to-concrete interactions, approximated throughout debonding mechanisms and dowel effects of fibers crossing cracks, are highlighted in Section 3.2. The mathematical critical condition for localized failure and its corresponding indicator for microplane-based constitutive models is developed in Section 4. In Section 5, the predictive capabilities and soundness of the proposal at constitutive level are addressed and compared against experimental results. Uniaxial tensile tests regarding variable fiber content, are evaluated in Section 5.1. A comparison against a discontinuous zero-thickness interface model is described in Section 5.2. Shear test are analyzed in Section 5.3. The influence of the considered microplanes number over the unit hemisphere has been evaluated in Section 5.3.1. The predictive capacity of the dowel mechanisms is verified in Section 5.3.2 and the localized failure indicator performance, in Section 5.3.3. Whereas in Section 5.4, the advantage of the inclusion of the elliptical CAP as a complement of the hyperbolic yield function is established by means of the discontinuous bifurcation analysis for uniaxial compression and combined shear/compression states. Section 5.5 deals with triaxial tests simulations for variable fiber content. Finally, some concluding remarks are outlined in Section 6.

17517648, 0, Downloaded from https://onlinelibrary.wiley.com/doi/10.1002/suco.202300875 by Antonio Caggiano - University Degli Studi Di , Wiley Online Library on [22/12/2024]. See the Terms and Conditions (https://onlinelibrary.wiley.com/terms-and-conditions) on Wiley Online Library for rules of use; OA articles are governed by the applicable Creative Commons License

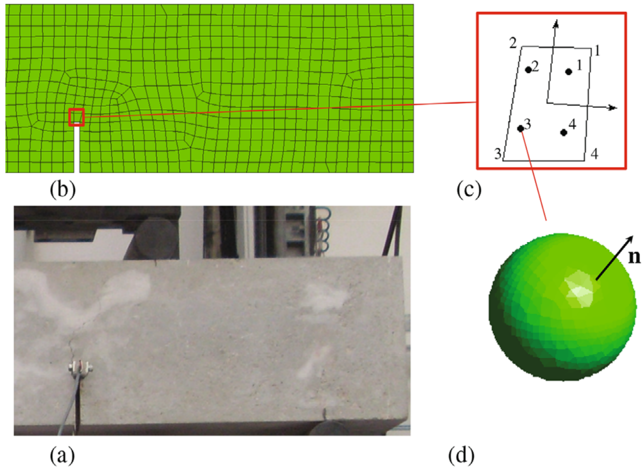

FIGURE 1 (a) Concrete specimen. (b) Continuum discretization scale. (c) 4-Node continuum FE. (d) Spherical microplane region at Gauss-point with a generalized normal direction.

2 | MICROPLANE THEORY: MAIN ASSUMPTIONS

The elasto-plastic microplane model developed for simulating the FRCC macroscopic failure behavior in a smeared crack mode, as shown Figure 1, follows the thermodynamically consistent formulation proposed by Carol et al.[21] and Kuhl et al.,[22] as summarized in this section.

Kinematic assumptions are considered based on Microplane Theory. Thus, micro-normal and shear strains (ε_N and $\boldsymbol{\varepsilon}_T$, respectively) are computed by means of the following projections

$$\varepsilon_N = \boldsymbol{N} : \boldsymbol{\varepsilon}, \quad \boldsymbol{\varepsilon}_T = \boldsymbol{T} : \boldsymbol{\varepsilon}, \tag{1}$$

with the projection tensors

$$\boldsymbol{N} = \boldsymbol{n} \bigotimes \boldsymbol{n}, \quad \boldsymbol{T} = \boldsymbol{n} \cdot \boldsymbol{I}^{\text{sym}} - \boldsymbol{n} \bigotimes \boldsymbol{n} \bigotimes \boldsymbol{n}, \tag{2}$$

being $\boldsymbol{I}^{\text{sym}}$ the symmetric part of the fourth-order identity tensor and $\boldsymbol{\varepsilon}$ the macroscopic strain tensor projected on a microplane characterized by its normal direction $\boldsymbol{n}$.

Assuming small strains, both macro- and microscopic strains are computed according to the Prandtl–Reuss additive decomposition. Thus, normal and tangential micro-strain rates are obtained as the addition of elastic and plastic components (denoted by supra-indexes e and p, respectively).

$$\dot{\varepsilon}_N = \dot{\varepsilon}_N^{\text{e}} + \dot{\varepsilon}_N^{\text{p}}, \quad \dot{\boldsymbol{\varepsilon}}_T = \dot{\boldsymbol{\varepsilon}}_T^{\text{e}} + \dot{\boldsymbol{\varepsilon}}_T^{\text{p}}. \tag{3}$$

A thermodynamically consistent homogenization between the field variables on the microplanes and the macroscopic ones is assured by applying the Clausius–Duhem inequality for isothermal processes, establishing that the macroscopic dissipation $\mathcal{D}^{\text{mac}}$, computed as the subtraction between the stress power $\boldsymbol{\sigma} \cdot \dot{\boldsymbol{\varepsilon}}$ and the evolution law of the free-energy per unit mass of material $\dot{\psi}^{\text{mac}}$, cannot become negative

$$\mathcal{D}^{\text{mac}} = \boldsymbol{\sigma} \cdot \dot{\boldsymbol{\varepsilon}} - \dot{\psi}^{\text{mac}} \geq 0, \tag{4}$$

being $\boldsymbol{\sigma}$ the macroscopic stress tensor. Computing the macro free-energy potential named ψ^{mac} as the integral of the micro free-energy ψ^{mic} on a spherical region of unit volume Ω, the micro–macro free-energy relationship is computed as

$$\psi^{\text{mac}} = \frac{3}{4\pi} \int_{\Omega} \psi^{\text{mic}} d\Omega. \tag{5}$$

The free-energy potential at microplane level is a function of the elastic strain components and the internal variable κ (scalar for isotropic hardening/softening behavior). Its evolution law, regarding the kinematic projection of Equation (1), results

$$\dot{\psi}^{\text{mic}} = \left(\sigma_N \boldsymbol{N} + \boldsymbol{T}^{\text{T}} \cdot \boldsymbol{\sigma}_T\right) : \dot{\boldsymbol{\varepsilon}} - \mathcal{D}^{\text{mic}}, \tag{6}$$

with the microscopic dissipation that satisfies the condition

$$\mathcal{D}^{\text{mic}} = -\frac{\partial \psi^{\text{mic}}}{\partial \kappa} \dot{\kappa} \geq 0. \tag{7}$$

The constitutive stresses at microplane level can be computed from their derivation as

$$\sigma_N = \frac{\partial \psi^{\text{mic}}}{\partial \varepsilon_N}, \quad \boldsymbol{\sigma}_T = \frac{\partial \psi^{\text{mic}}}{\partial \boldsymbol{\varepsilon}_T}, \quad \phi = \frac{\partial \psi^{\text{mic}}}{\partial \kappa}, \tag{8}$$

being ϕ the dissipative micro-stresses.

The macroscopic stress tensor in terms of the microscopic stress components can be computed according to Coleman and Noll[35] and Coleman and Gurtin,[36] regarding the Clausius–Duhem inequality of Equation (4), as

$$\boldsymbol{\sigma} = \frac{\partial \psi^{\text{mac}}}{\partial \boldsymbol{\varepsilon}} = \frac{3}{4\pi} \int_{\Omega} \sigma_N \boldsymbol{N} + \boldsymbol{T}^{\text{T}} \cdot \boldsymbol{\sigma}_T d\Omega. \tag{9}$$

Due to the complexity of the analytic solution of this equation, it is usually solved in numerical form by the proposal from Bažant and Oh[37] as

17517648, 0, Downloaded from https://onlinelibrary.wiley.com/doi/10.1002/suco.202300875 by Antonio Caggiano - University Degli Studi Di , Wiley Online Library on [22/12/2024]. See the Terms and Conditions (https://onlinelibrary.wiley.com/terms-and-conditions) on Wiley Online Library for rules of use; OA articles are governed by the applicable Creative Commons License

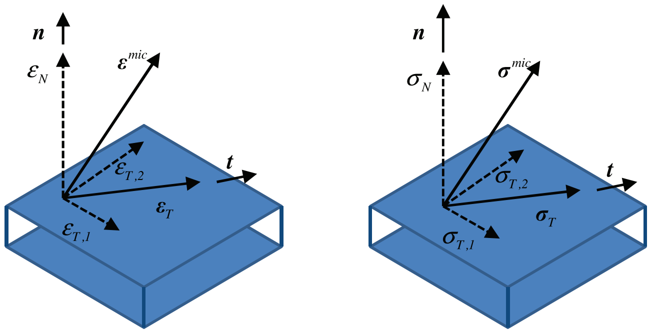

FIGURE 2 Strain and stress components at the microplane level.

$$\boldsymbol{\sigma} \approx \sum_{I=1}^{n_{\mathrm{mp}}} \left[\boldsymbol{N}^I \sigma_N^I + \boldsymbol{T}^{\mathrm{T},I} \cdot \boldsymbol{\sigma}_T^I \right] \mathbf{w}^I, \tag{10}$$

where n_{mp} denotes the adopted number of microplanes and $\mathbf{w}^I$ the corresponding weight coefficients.

Figure 2 shows the microplane strain $\boldsymbol{\varepsilon}^{\mathrm{mic}}$ and stress vectors $\boldsymbol{\sigma}^{\mathrm{mic}}$, whose components in correspondence with the projections on the microplane direction $\boldsymbol{n}$ and its orthogonal $\boldsymbol{t}$, are given by $\boldsymbol{\varepsilon}^{\mathrm{mic}} = [\varepsilon_N \ \varepsilon_{T,1} \ \varepsilon_{T,2}]^{\mathrm{T}}$ and $\boldsymbol{\sigma}^{\mathrm{mic}} = [\sigma_N \quad \sigma_{T,1} \quad \sigma_{T,2}]^{\mathrm{T}}$.

3 | COMPOSITE CONSTITUTIVE FORMULATION FOR FRCC

The proposed microplane constitutive model for FRCC is formulated by means of the combination of three internal constitutive laws, whose main features are detailed in the following sections and are briefly outlined below:

1. *Fracture energy-based plasticity formulation for plain cementitious matrix*, relating normal and tangential microplane stress components with their corresponding micro-strains. Two combined failure criteria are considered: (i) a maximum strength function defined in terms of a three-parameter hyperbolic criterion by Carol et al.[38] and (ii) a novel elliptical CAP surface for high negative values of normal stress (high compression). Post-cracking behavior is controlled in terms of plastic work spent. A non-associated flow rule is adopted to complete the constitutive material model for the hyperbolic sector, while a fully-associated plastic flow law is considered for the CAP formulation.
2. *Bridging effect of fibers loaded in tension*, involving the bond–slip interaction between fibers and matrix.
3. *Dowel action of fibers in concrete cracks*, based on elastic beam foundation concepts, to characterize the shear transfer mechanism of fibers crossing cracks. The dowel strength represents a relevant contribution in case of steel fibers and can be mainly neglected in case of plastic reinforcements.

FRCC is modeled as a composite material made of a cementitious matrix and randomly oriented reinforcements. According to the basis of the Mixture Theory, the following hypotheses are considered: (i) each infinitesimal volume is simultaneously occupied by all constituents, (ii) assuming a parallel mechanical system, in every infinitesimal volume, the kinematic field of the equivalent continuum, and that one of each mixture constituent, agree, (iii) the corresponding composite stress field is given by the weighted sum (in terms of the volume fraction) of the constituent stresses, according to

$$\boldsymbol{\sigma}^{\mathrm{mic}} = \rho_{\mathrm{m}} \boldsymbol{\sigma}^{\mathrm{m}} + \sum_{f=0}^{n_f} \rho_{\mathrm{f}} \left[\sigma_N^{\mathrm{f}}(\varepsilon_N) \boldsymbol{n} + \boldsymbol{\sigma}_T^{\mathrm{f}}(\boldsymbol{\varepsilon}_T) \cdot \boldsymbol{t} \right], \tag{11}$$

being ρ_{m} and ρ_{f} the weighting functions depending on the volume fraction of each constituent, m and f deal with the mortar and fiber indices, respectively; σ_N^{f} and $\boldsymbol{\sigma}_T^{\mathrm{f}}$ mean the bond–slip and dowel actions of the single considered fiber which are related to its axial and tangential strains, ε_N and $\boldsymbol{\varepsilon}_T$, respectively. Finally, $\boldsymbol{n}$ and $\boldsymbol{t}$ denote the fiber direction and its orthogonal, respectively.

The evaluation of the total number of fibers crossing each microplane, represented by n_{f}, is calculated adopting the proposals given by Krenchel[39] and Dupont and Vandewalle[40] as

$$n_{\mathrm{f}} = \alpha_N \frac{\rho_{\mathrm{f}}}{A_{\mathrm{f}}} A_{\mathrm{i}}, \tag{12}$$

where α_N the orientation factor (assuming the value of 0.405 according to Soroushian and Lee[41]), while A_{f} and A_{i} are single fiber and interface cross-sectional areas, respectively.

3.1 | Fracture energy model for cementitious composite

The inelastic model that describes the failure behavior for a cementitious composite matrix (as the case of plain concrete) is outlined in this section.

17517648, 0, Downloaded from https://onlinelibrary.wiley.com/doi/10.1002/suco.202300875 by Antonio Caggiano - University Degli Studi Di , Wiley Online Library on [22/12/2024]. See the Terms and Conditions (https://onlinelibrary.wiley.com/terms-and-conditions) on Wiley Online Library for rules of use; OA articles are governed by the applicable Creative Commons License

Fully uncoupled normal/tangential material laws are defined at the microplane level, that is, the normal and the tangential stress components are given as the conjugate components to the corresponding microplane strains according to Equation (8) and their evolutions are computed regarding the additive decomposition of Equation (3), as

$$\dot{\sigma}_N^{\mathrm{m}} = E_N\left(\dot{\varepsilon}_N - \dot{\varepsilon}_N^{\mathrm{p}}\right), \quad \dot{\boldsymbol{\sigma}}_T^{\mathrm{m}} = E_T\left(\dot{\boldsymbol{\varepsilon}}_T - \dot{\boldsymbol{\varepsilon}}_T^{\mathrm{p}}\right), \tag{13}$$

where E_N and E_T are the microscopic elastic stiffnesses, defined according to Leukart,[42] consistently with the macroscopic elastic constitutive relationship $\boldsymbol{\sigma} = \boldsymbol{E} : \boldsymbol{\varepsilon}$, with the elastic tensor $\boldsymbol{E}$ computed as

$$\boldsymbol{E} = 3K\boldsymbol{I}^{\mathrm{vol}} + 2G\boldsymbol{I}^{\mathrm{dev}}, \tag{14}$$

where K and G represents the bulk and shear macroscopic modules, respectively, whereas $\boldsymbol{I}^{\mathrm{vol}} = 1/3\boldsymbol{I} \bigotimes \boldsymbol{I}$ and $\boldsymbol{I}^{\mathrm{dev}} = \boldsymbol{I}^{\mathrm{sym}} - \boldsymbol{I}^{\mathrm{vol}}$ denote the volumetric and deviatoric part of the fourth-order unit tensor, respectively.

The elastic material tensor can be specified as a function of the elastic stiffnesses of the micro level, as

$$\boldsymbol{E} = \frac{3}{4\pi}\int_{\Omega} E_N \boldsymbol{N}^{\mathrm{T}} \bigotimes \boldsymbol{N} + E_T \boldsymbol{T}^{\mathrm{T}} \cdot \boldsymbol{T} d\Omega. \tag{15}$$

Regarding that projection tensors have useful integration properties for the homogenization of the microscopic response on the macro-level, reported by Kanatani[43] and Lubarda and Krajcinovic,[44] as

$$\begin{aligned} &\frac{3}{4\pi}\int_{\Omega} \boldsymbol{N}^{\mathrm{T}} \bigotimes \boldsymbol{N} d\Omega = \boldsymbol{I}^{\mathrm{vol}} + \frac{2}{5}\boldsymbol{I}^{\mathrm{dev}}, \\ &\frac{3}{4\pi}\int_{\Omega} \boldsymbol{T}^{\mathrm{T}} \cdot \boldsymbol{T} d\Omega = \frac{3}{5}\boldsymbol{I}^{\mathrm{dev}}, \end{aligned} \tag{16}$$

and substituting Equations (16) in (15), the normal and tangential elastic modules result

$$E_N = 3K \quad \text{and} \quad E_T = \frac{10}{3G} - 2K. \tag{17}$$

The stress rate vector $\dot{\boldsymbol{\sigma}}^{\mathrm{mic}} = \left[\dot{\sigma}_N^{\mathrm{m}} \;\; \dot{\sigma}_{T,1}^{\mathrm{m}} \;\; \dot{\sigma}_{T,2}^{\mathrm{m}}\right]^{\mathrm{T}}$ and the rate of the microplane elastic strains $\dot{\boldsymbol{\varepsilon}}^{\mathrm{mic,e}} = \left[\dot{\varepsilon}_N^{\mathrm{m,e}} \;\; \dot{\varepsilon}_{T,1}^{\mathrm{m,}}\right.$ $\left.\mathrm{e}\dot{\varepsilon}_{T,2}^{\mathrm{m,e}}\right]^{\mathrm{T}}$ are connected by means of the following elastic stiffness operator

$$\boldsymbol{C}^{\mathrm{mic}} = \begin{pmatrix} E_N & 0 & 0 \\ 0 & E_T & 0 \\ 0 & 0 & E_T \end{pmatrix}, \tag{18}$$

then

$$\dot{\boldsymbol{\sigma}}^{\mathrm{mic}} = \boldsymbol{C}^{\mathrm{mic}} \cdot \dot{\boldsymbol{\varepsilon}}^{\mathrm{mic,e}}, \quad \dot{\boldsymbol{\sigma}}^{\mathrm{mic}} = \boldsymbol{C}^{\mathrm{mic}} \cdot \left(\dot{\boldsymbol{\varepsilon}}^{\mathrm{mic}} - \dot{\boldsymbol{\varepsilon}}^{\mathrm{mic,p}}\right). \tag{19}$$

The evolution laws of the plastic strain components and the internal variable are computed under consideration of a convex yield function $F\left(\boldsymbol{\sigma}^{\mathrm{mic}}\right)$ and a plastic potential $Q\left(\boldsymbol{\sigma}^{\mathrm{mic}}\right)$ according to the plasticity flow theory, as

$$\dot{\varepsilon}_N^{\mathrm{m,p}} = \dot{\lambda}\frac{\partial Q}{\partial \sigma_N^{\mathrm{m}}}, \quad \dot{\boldsymbol{\varepsilon}}_T^{\mathrm{m,p}} = \dot{\lambda}\frac{\partial Q}{\partial \left\|\sigma_T^{\mathrm{m}}\right\|}, \quad \dot{\kappa} = \dot{\lambda}\frac{\partial Q}{\partial \phi}, \tag{20}$$

where $\dot{\lambda}$ is the evolution of the non-negative plastic multiplier derived by means of the classical Kuhn-Tucker and consistency conditions

$$\dot{\lambda} \geq 0, \quad F\left(\boldsymbol{\sigma}^{\mathrm{mic}}\right) \leq 0, \quad \dot{\lambda} \;\; F\left(\boldsymbol{\sigma}^{\mathrm{mic}}\right) = 0, \quad \dot{F}\left(\boldsymbol{\sigma}^{\mathrm{mic}}\right) = 0. \tag{21}$$

The adopted failure criterion, shown in Figure 3, is given on each microplane stress-space as a function of three material parameters: that is, the tensile strength χ^{mic}, the cohesion c^{mic} and the internal friction angle ϕ^{mic}. Its expression is represented by the hyperbola by Carol et al.,[38] when $\sigma_N^{\mathrm{m}} \geq \sigma_{N,\mathrm{CAP}}$, as

$$\begin{aligned} F\left(\boldsymbol{\sigma}^{\mathrm{mic}}\right) = \left\|\boldsymbol{\sigma}_T^{\mathrm{m}}\right\|^2 - \left[c^{\mathrm{mic}} - \sigma_N^{\mathrm{m}} \tan\left(\phi^{\mathrm{mic}}\right)\right]^2 + \Big[c^{\mathrm{mic}} \\ - \chi^{\mathrm{mic}} \tan\left(\phi^{\mathrm{mic}}\right)\Big]^2 \leq 0. \end{aligned} \tag{22}$$

On the contrary, if $\sigma_N^{\mathrm{m}} < \sigma_{N,\mathrm{CAP}}$, the following elliptical function is taken into account

$$F\left(\boldsymbol{\sigma}^{\mathrm{mic}}\right) = \left\|\boldsymbol{\sigma}_T^{\mathrm{m}}\right\|^2 - \frac{1}{R_{\mathrm{CAP}}^2}\left[\left(\sigma_N^{\mathrm{m}} - \sigma_{N,0}\right)^2 - \left(\sigma_{N,\mathrm{CAP}} - \sigma_{N,0}\right)^2\right] \leq 0, \tag{23}$$

where R_{CAP}, $\sigma_{N,\mathrm{CAP}}$, and $\sigma_{N,0}$ are model parameters. Particularly, $\sigma_{N,\mathrm{CAP}}$ represents the value of σ_N^{m} situated on the boundary between the hyperbola and the ellipse. In this way, the continuity of the tangent at the intersections of the hyperbola and the ellipse is ensured, see Caggiano[45] for more explanations.

The plastic flow rule, defining the direction of inelastic strains, is also represented by two parts: (i) a general non-associated law, corresponding with the hyperbolic model section and (ii) a full-associated one for the elliptical CAP formulation.

In zero-thickness interface models for heterogeneous materials such as concrete or rock, controlling dilatancy is crucial for accurately reproducing fracture phenomena. Dilatancy refers to the tendency of two faces of a modeled

17517648, 0, Downloaded from https://onlinelibrary.wiley.com/doi/10.1002/suco.202300875 by Antonio Caggiano - University Degli Studi Di , Wiley Online Library on [22/12/2024]. See the Terms and Conditions (https://onlinelibrary.wiley.com/terms-and-conditions) on Wiley Online Library for rules of use; OA articles are governed by the applicable Creative Commons License

crack, under zero or low normal compression, to dilate during sliding. This behavior is due to the well-known "saw tooth" effect caused by the meso-scale material heterogeneity of the crack front. As compression increases, dilatancy gradually decreases and eventually disappears under very high confinement.[46] Furthermore, dilatancy can reduce as sliding progresses and the crack surface degrades through the fracture process,[47,48] becoming necessary the use of non-associated flow rules to correctly model mixed fracture modes. In pure compaction (i.e., inverse direction to mode I), the flow rule for joint models must be consistently fully associated. For this reason, the same hypothesis is adopted in the CAP zone.

Regarding the rate of the plastic strains of Equation (20), the components of the derived vectors can be reached by means of the transformation operator $\boldsymbol{A}^{\text{mic}}$, applied to the normal flow direction as

$$\left[\frac{\partial Q}{\partial \sigma_N^{\text{m}}}, \frac{\partial Q}{\partial \|\boldsymbol{\sigma}_T^{\text{m}}\|}\right]^{\text{T}} = \boldsymbol{A}^{\text{mic}}\left[\frac{\partial F}{\partial \sigma_N^{\text{m}}}, \frac{\partial F}{\partial \|\boldsymbol{\sigma}_T^{\text{m}}\|}\right] \tag{24}$$

being

$$\text{Hyperbola}: \quad \boldsymbol{A} = \begin{cases} \begin{pmatrix} \dfrac{\tan(\beta^{\text{mic}})}{\tan(\phi^{\text{mic}})} & 0 \\ 0 & 1 \end{pmatrix} & \text{if} \quad \sigma_N^{\text{m}} \geq 0 \\ \begin{pmatrix} \left[1 - \dfrac{|\sigma_N^{\text{m}}|}{\sigma_{\text{dil}}^{\text{mic}}}\right] \dfrac{\tan(\beta^{\text{mic}})}{\tan(\phi^{\text{mic}})} & 0 \\ 0 & 1 \end{pmatrix} & \text{if} \quad -\sigma_{\text{dil}}^{\text{mic}} \leq \sigma_N^{\text{m}} < 0 \\ \begin{pmatrix} 0 & 0 \\ 0 & 1 \end{pmatrix} & \text{if} \quad \sigma_{N,\text{CAP}} \leq \sigma_N^{\text{m}} < -\sigma_{\text{dil}}^{\text{mic}} \end{cases} \tag{25}$$

$$\text{Elliptical formulation}: \quad \boldsymbol{A} = \begin{pmatrix} 1 & 0 \\ 0 & 1 \end{pmatrix} \quad \text{if} \quad \sigma_N^{\text{m}} < \sigma_{N,\text{CAP}} \tag{26}$$

In Equation (25), $\tan(\beta^{\text{mic}})$ represents the dilation angle of the plastic potential, as depicted in Figure 3: $0 \leq \tan(\beta^{\text{mic}}) \leq \tan(\phi^{\text{mic}})$. Thereby, the parameter $\sigma_{\text{dil}}^{\text{mic}}$ represents the normal stress at which the dilatancy vanishes.[38,49] Moreover, Equation (26) deals with the associated flow direction characterizing the elliptical CAP model.

Three main fracture mechanisms govern the post-cracking evolution:

1. Mode I type of fracture reached along the horizontal axis of the failure criterion in the tensile region.
2. Shear fracture modes (the mode II type) with compression stress ranges.
3. Pure compaction mode along the horizontal axis of the failure criterion in the elliptical CAP negative region.

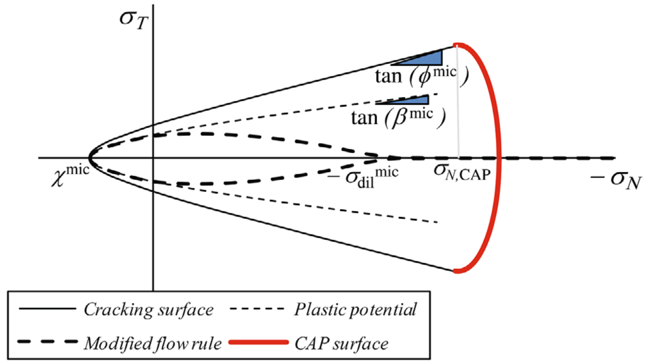

FIGURE 3 Maximum strength criterion and plastic flow rules.

The evolution of the model parameters in softening regime is driven by means of the following expression

$$p_i^{\text{mic}} = \left(1 - \left(1 - r_p^{\text{mic}}\right) S\left(\xi_{p_i^{\text{mic}}}\right)\right) p_{0i}^{\text{mic}}, \tag{27}$$

where p_i^{mic} represents any of these parameters: χ^{mic}, c^{mic}, $\tan(\phi^{\text{mic}})$ (hyperbolic function) and $\sigma_{N,\text{CAP}}$ (ellipse). These model parameters vary from their maximum values p_{0i}^{mic} to the corresponding residual ones $r_p^{\text{mic}} p_{0i}^{\text{mic}}$.

The ratio between the work spent in fracture w_{cr} and the corresponding fracture energy parameters, G_{f}^{I} (defining the fracture energy released in pure mode I) and $G_{\text{f}}^{\text{IIa}}$ (dealing with the fracture energy for the asymptotic mode II), defines a unified scaling parameter $S\left(\xi_{p_i^{\text{mic}}}\right)$, as introduced by Carol et al.[38]

$$S\left(\xi_{p_i^{\text{mic}}}\right) = \frac{\mathrm{e}^{-\alpha p_i} \xi_{p_i^{\text{mic}}}}{1 + (\mathrm{e}^{-\alpha_{p_i}} - 1)\xi_{p_i^{\text{mic}}}}, \tag{28}$$

where the parameter α_{p_i} controls the decay form of the internal parameter as shown in Figure 4. The nondimensional variable $\xi_{\#} = \xi_{p_i^{\text{mic}}}(w_{\text{cr}}/G_{\text{f}}^{\#})$ introduces the influence of the ratio between the current fracture work spent and the available fracture energy as follows

$$\xi_{\chi^{\text{mic}}} = \begin{cases} \dfrac{1}{2}\left[1 - \cos\left(\dfrac{\pi w_{\text{cr}}}{G_{\text{f}}^{\text{I}}}\right)\right] & \text{if } w_{\text{cr}} \leq G_{\text{f}}^{\text{I}} \\ 1 & \text{otherwise} \end{cases} \tag{29}$$

$$\xi_{c^{\text{mic}}} = \xi_{\tan(\phi^{\text{mic}})} = \xi_{\sigma_{N,\text{CAP}}} = \begin{cases} \dfrac{1}{2}\left[1 - \cos\left(\dfrac{\pi w_{\text{cr}}}{G_{\text{f}}^{\text{IIa}}}\right)\right] & \text{if } w_{\text{cr}} \leq G_{\text{f}}^{\text{IIa}} \\ 1 & \text{otherwise} \end{cases} \tag{30}$$

according to the function proposed by Caballero et al.[50] Figure 5 shows the typical curves obtained with Equations (29) or (30).

17517648, 0, Downloaded from https://onlinelibrary.wiley.com/doi/10.1002/suco.202300875 by Antonio Caggiano - University Degli Studi Di , Wiley Online Library on [22/12/2024]. See the Terms and Conditions (https://onlinelibrary.wiley.com/terms-and-conditions) on Wiley Online Library for rules of use; OA articles are governed by the applicable Creative Commons License

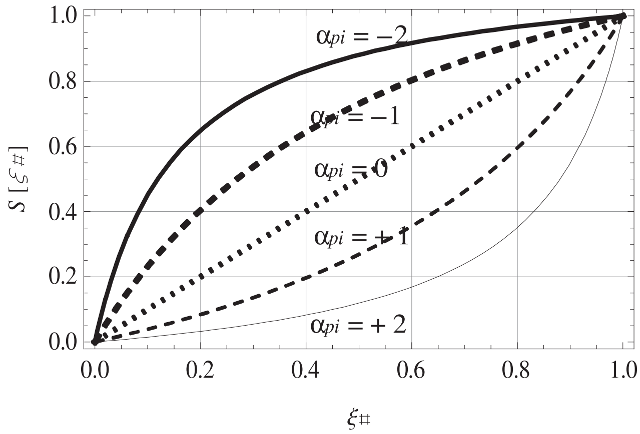

FIGURE 4 $S(\xi_\#)$ scaling function of the microplane model in terms of the $\xi_\#$ parameter, where the # symbol $=\chi^{\mathrm{mic}}, c^{\mathrm{mic}}$, $\tan(\phi^{\mathrm{mic}})$, or $\sigma_{N,\mathrm{CAP}}$.

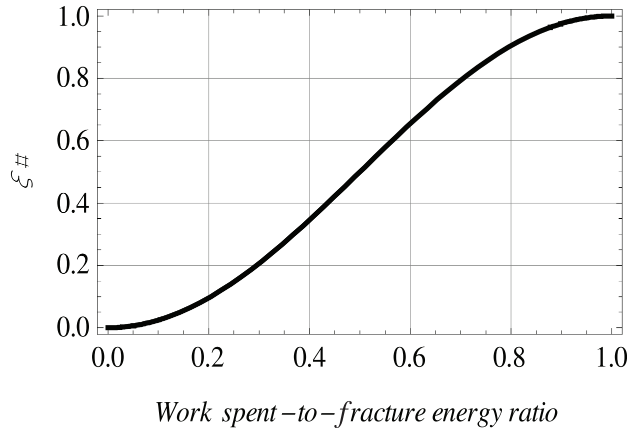

FIGURE 5 $\xi_\#$ functions, with $\# = \chi^{\mathrm{mic}}, c^{\mathrm{mic}}$, $\tan(\alpha^{\mathrm{mic}})$ or $\sigma_{N,\mathrm{CAP}}$, depending on the work spent-to-fracture energy ratio, $w_{\mathrm{cr}}/G_{\mathrm{f}}^{\mathrm{I}}$ or $w_{\mathrm{cr}}/G_{\mathrm{f}}^{\mathrm{IIa}}$.

In order to illustrate the main features of the proposed yielding surfaces and their evolutions, based on Equations (28)–(30), various plot examples are reported in Figure 6. The numerical values considered in these examples for the relevant mechanical parameters are: the initial strength values $\chi_0^{\mathrm{mic}} = 1.0\,\mathrm{MPa}$, $c_0^{\mathrm{mic}} = 1.0\,\mathrm{MPa}$, $\tan(\phi_0^{\mathrm{mic}}) = 0.3$ and $\sigma_{N,\mathrm{CAP}_0} = -1.0\,\mathrm{MPa}$; the residual strengths $\chi_r^{\mathrm{mic}} = 0.0\,\mathrm{MPa}$, $c_r^{\mathrm{mic}} = 0.0\,\mathrm{MPa}$, $\tan(\phi_r^{\mathrm{mic}}) = 0.1$ and $\sigma_{N,\mathrm{CAP}_r} = -0.1$ MPa; and all the shape coefficients $\alpha_{p_i} = 0.0$.

The rate of the plastic work $\dot{w}_{\mathrm{cr}}$ is given by means of the following expressions, depending on the σ_N^{m} value, as

$$\begin{aligned}
\dot{w}_{\mathrm{cr}} &= \sigma_N^{\mathrm{m}} \cdot \dot{\varepsilon}_N^{\mathrm{p}} \cdot l_{\mathrm{cs}}^{\mathrm{I}} + \sigma_{T,k}^{\mathrm{m}} \cdot \dot{\varepsilon}_{T,k}^{\mathrm{m,p}} \cdot l_{\mathrm{cs}}^{\mathrm{II}} \quad \text{if } \sigma_N^{\mathrm{m}} < \sigma_{N,\mathrm{CAP}} \text{ or } \sigma_N^{\mathrm{m}} \geq 0 \\
\dot{w}_{\mathrm{cr}} &= \sigma_{T,k}^{\mathrm{m}} \cdot \dot{\varepsilon}_{T,k}^{\mathrm{m,p}} \cdot l_{\mathrm{cs}}^{\mathrm{II}} \left(1 - \frac{|\sigma_N^{\mathrm{m}}| \tan(\phi^{\mathrm{mic}})}{\|\sigma_T^{\mathrm{m}}\|}\right) \quad \text{if } \sigma_{N,\mathrm{CAP}} \leq \sigma_N^{\mathrm{m}} < 0
\end{aligned} \tag{31}$$

in which the strain components on each microplane, $\boldsymbol{\varepsilon}^{\mathrm{mic}} = \left[\varepsilon_N^{\mathrm{m}} \;\; \varepsilon_{T_1}^{\mathrm{m}} \;\; \varepsilon_{T_2}^{\mathrm{m}}\right]^{\mathrm{T}}$, can be easily transformed in terms of the crack-opening displacement through the following expressions

$$\varepsilon_N^{\mathrm{m}} = \frac{u}{l_{\mathrm{cs}}^{\mathrm{I}}}, \quad \varepsilon_{T_1}^{\mathrm{m}} = \frac{v_1}{l_{\mathrm{cs}}^{\mathrm{IIa}}}, \quad \varepsilon_{T_2}^{\mathrm{m}} = \frac{v_2}{l_{\mathrm{cs}}^{\mathrm{IIa}}}, \tag{32}$$

where u, v_1, and v_2 are the relative crack displacements, while $l_{\mathrm{cs}}^{\mathrm{I}}$ and $l_{\mathrm{cs}}^{\mathrm{IIa}}$ are homogenization characteristic lengths to be calibrated for the considered failure modes. They mainly represent the crack spacings in direct tension and under shear stress states with very high confinement, or the damaged zone under compressive compaction, respectively.

3.2 | Crack-bridging effect and dowel action of fibers

This section deals with fiber actions deriving from fracture opening processes in cementitious matrix, schematically showed in Figure 7, that take relevant bridging effects on the FRCC constitutive response.

On the one hand, the bond mechanism between fibers and cementitious matrix is taken into account as an axial (tensile) stress σ_N^{f} acting at the microplanes. It can be derived by equilibrium conditions of shear stresses reacting on the lateral contact surfaces of fibers embedded within the concrete matrix as outlined in Figure 7. On the other hand, the dowel action V_{d} as result of the shear transfer mechanism, represents another important component on the overall bridging effect of fibers in fracture processes of FRCC.

The constitutive formulations for both bond–slip and dowel mechanisms are summarized in Table 1. One-dimensional elasto-plastic constitutive relations are considered, whereas Rankine-type functions have been adopted to describe the corresponding yield functions.

The material mechanical features of the bond–slip model have been computed by Oliver et al.[33] regarding a serial system whereby the fiber total strain $\varepsilon_N^{\mathrm{f}}$ is assumed as the sum of the proper fiber deformation and the interface sliding. Whereas the normal fiber stress σ_N^{f} is identical on each component. E^{f} and σ_y^{f} are the equivalent elastic modulus and yield stress, respectively, and H_N^{f} the hardening/softening parameter, whereas κ_N^{f} is the internal variable, conjugated to the dissipative stress ϕ_N^{f}.

Besides, the adopted dowel stiffness G^{f} and the equivalent strength τ_y^{f} characterizing the dowel mechanism, are based on the definition of both stiffness and strength

17517648, 0, Downloaded from https://onlinelibrary.wiley.com/doi/10.1002/suco.202300875 by Antonio Caggiano - University Degli Studi Di , Wiley Online Library on [22/12/2024]. See the Terms and Conditions (https://onlinelibrary.wiley.com/terms-and-conditions) on Wiley Online Library for rules of use; OA articles are governed by the applicable Creative Commons License

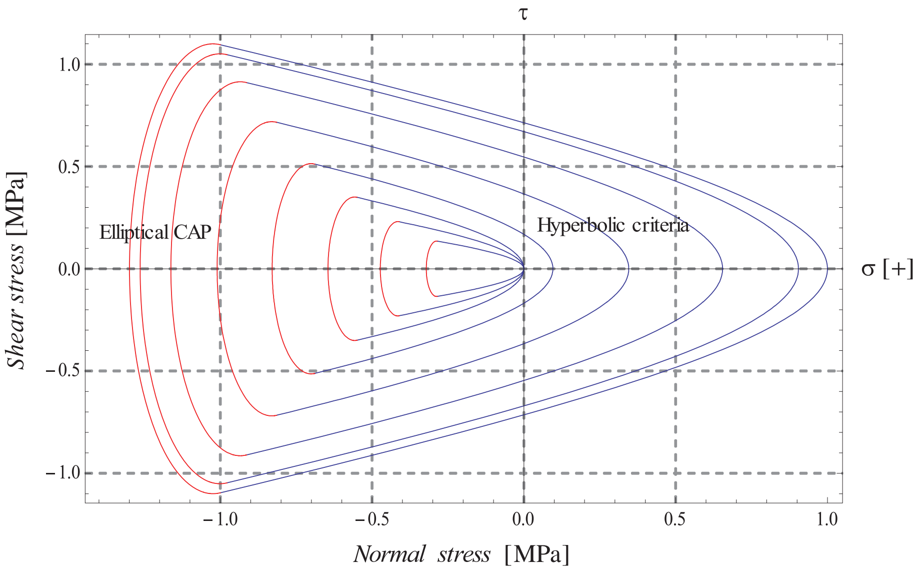

FIGURE 6 Yielding criteria at different ratios between work spent values and fracture energies: $\left(\frac{w_{cr}}{G_f^{I}}, \frac{w_{cr}}{G_f^{IIa}}\right) = (0.0, 0.0), (0.2, 0.1), (0.4, 0.2), (0.6, 0.3), (0.8, 0.4), (1.0, 0.5), (1.0, 0.6), (1.0, 0.8)$ (from the biggest size up to smallest one).

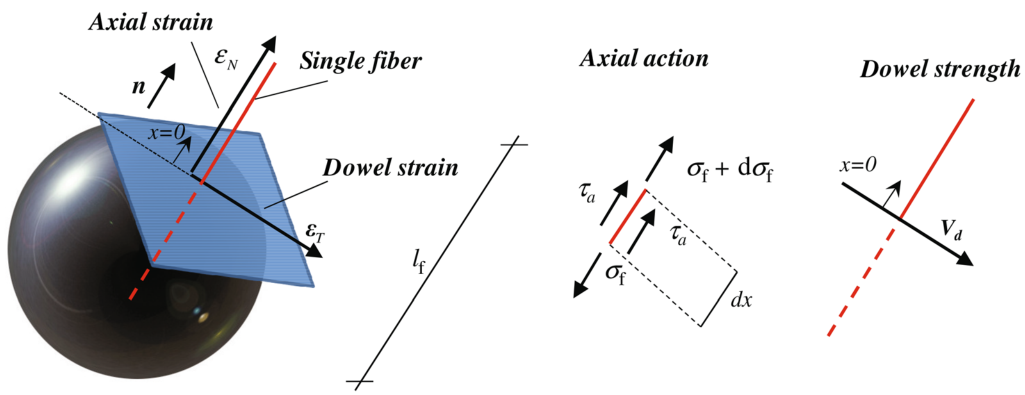

FIGURE 7 Microplane strain activating the fiber bridging effects.

TABLE 1 Summary of the constitutive formulation for fibers.

	Bond–slip	Dowel action
Constitutive relation	$\sigma_N^f = E^f\left(\varepsilon_N^f - \varepsilon_N^{f,p}\right)$	$\boldsymbol{\sigma}_T^f = G^f\left(\boldsymbol{\varepsilon}_T^f - \boldsymbol{\varepsilon}_T^{f,p}\right)$
Yield function	$F_N^f = \sigma_N^f - \left(\sigma_y^f + \phi_N^f\right) \le 0$	$F_T^f = \lVert\sigma_T^f\rVert - \left(\tau_y^f + \phi_T^f\right) \le 0$
Internal variable evolution	$\dot{\kappa}_N^f = \dot{\lambda}_N^f$	$\dot{\kappa}_T^f = \dot{\lambda}_T^f$
Softening law	$\dot{\phi}_N^f = H_N^f \dot{\kappa}_N^f$	$\dot{\phi}_T^f = H_T^f \dot{\kappa}_T^f$

of a generic fiber embedded in a concrete matrix and subjected to a transverse force.[51–54] Moreover, κ_N^f represents the internal variable conjugated to the dissipative stress ϕ_T^f and H_T^f, once again, the hardening/softening parameter.

For the sake of brevity, many details of the model derivations have been omitted. The complete formulations for both bond–slip and dowel action has completely been detailed in Vrech et al.[27]

4 | ANALYTICAL SOLUTION FOR LOCALIZED FAILURE IN MICROPLANE-BASED ELASTO-PLATICITY

The inhomogeneous or localized deformation field in the realm of the SCA exhibits a plane of discontinuity characterized by its normal direction $\boldsymbol{N}_d$, that can be identified by means of the eigenvalue problem of the acoustic or

17517648, 0, Downloaded from https://onlinelibrary.wiley.com/doi/10.1002/suco.202300875 by Antonio Caggiano - University Degli Studi Di , Wiley Online Library on [22/12/2024]. See the Terms and Conditions (https://onlinelibrary.wiley.com/terms-and-conditions) on Wiley Online Library for rules of use; OA articles are governed by the applicable Creative Commons License

localization tensor, related to discontinuous bifurcations of the equilibrium path, leading to lost of ellipticity of the equations that govern the static equilibrium problem. For further explanations on the deduction of the localized failure indicator, see Appendix A.

The elasto-plastic acoustic tensor for microplane-based plasticity, is computed in a similar way to Equation (10), as

$$\boldsymbol{Q}^{\mathrm{ep}} \approx \boldsymbol{Q}^{\mathrm{e}} - \sum_{I=1}^{n_{\mathrm{mp}}} \left[\frac{\boldsymbol{a}^{*I} \otimes \boldsymbol{a}^{I}}{h^{I}} \right] \mathbf{w}^{I}, \tag{33}$$

being $\boldsymbol{Q}^{\mathrm{e}} = \boldsymbol{N}_{\mathrm{d}} \cdot \boldsymbol{E}^{\mathrm{e}} \cdot \boldsymbol{N}_{\mathrm{d}}$ the elastic acoustic tensor, h^{I} the generalized softening modulus and the traction vectors computed as

$$\boldsymbol{a}^{\mathrm{I}} = \left[\frac{\partial F}{\partial \sigma_N} E_N \boldsymbol{N} + E_T \frac{\partial F}{\partial \boldsymbol{\sigma}_T} \cdot \boldsymbol{T} \right] \cdot \boldsymbol{N}_{\mathrm{d}}, \tag{34}$$

$$\boldsymbol{a}^{*\mathrm{I}} = \boldsymbol{N}_{\mathrm{d}} \cdot \left[E_N \frac{\partial Q}{\partial \sigma_N} \boldsymbol{N} + E_T \boldsymbol{T}^{\mathrm{T}} \cdot \frac{\partial Q}{\partial \boldsymbol{\sigma}_T} \right]. \tag{35}$$

The localization condition in Equation (33) serves as a basis for numerical evaluations of the associated localization directions for any possible stress history.

5 | NUMERICAL ANALYSIS OF THE FAILURE AT MATERIAL LEVEL

This section is intended to evaluate the numerical stability of the developed formulation as well as to demonstrate the capabilities of the proposed constitutive theory at material level, regarding FRCC under typical loading states and comparing numerical results against experimental data available in literature. With this purpose, each material point is represented by a single quadrilateral 4-nodes finite element, consisting of 4 Gauss-points, as shown in Figure 1. A variable number of microplanes has been considered on each Gauss-point as indicated in each subsection. The schematized test cases reported in Figure 8, and by considering cubic samples of SFRC under plane stress condition, are evaluated. Internal parameters have been adjusted via iterative calibration by comparing model predictions against experimental data (e.g., stress–strain curves and failure mechanisms).

In the following subsections, basic tests have been simulated with specific objectives:

- Uniaxial tensile test in Section 5.1. Comparison of numerical results against experimental data by Li and Li[55] in terms of Tensile stresses versus Strains curves for both plain concrete and SFRC with uniform distribution of fibers, under plane stress condition by considering 41 microplanes.
- In Section 5.2, numerical Load versus Displacement curves regarding variable microplanes number are compared with those of the zero-thickness interface model by Caggiano et al.,[15] with the aim to demonstrate the versatility of the proposed method. To this end, the plane microplane formulation by Park and Kim[56] has been applied.
- Section 5.3 deals with simple shear tests:
  - Stating the minimum microplanes number for an acceptable accuracy in Section 5.3.1.

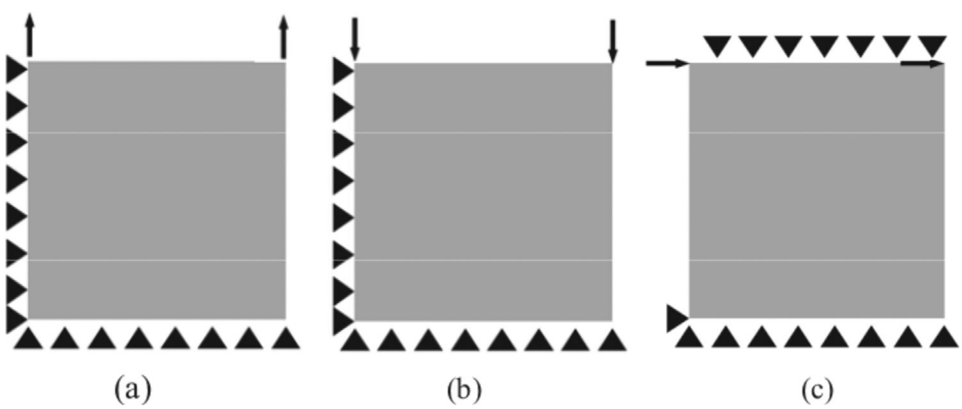

FIGURE 8 Boundary conditions of: (a) uniaxial tensile; (b) compression; (c) shear with constrained dilatancy tests.

TABLE 2 Fiber types employed in the experimental campaign by Li and Li.[55]

	Density [g/cm^3]	d_f [mm]	l_f [mm]	σ_y^s [GPa]	E^s [GPa]
Dramix type I	7.8	0.5	30	1.20	200
Dramix type II	7.8	0.5	50	1.20	200

17517648, 0, Downloaded from https://onlinelibrary.wiley.com/doi/10.1002/suco.202300875 by Antonio Caggiano - University Degli Studi Di , Wiley Online Library on [22/12/2024]. See the Terms and Conditions (https://onlinelibrary.wiley.com/terms-and-conditions) on Wiley Online Library for rules of use; OA articles are governed by the applicable Creative Commons License

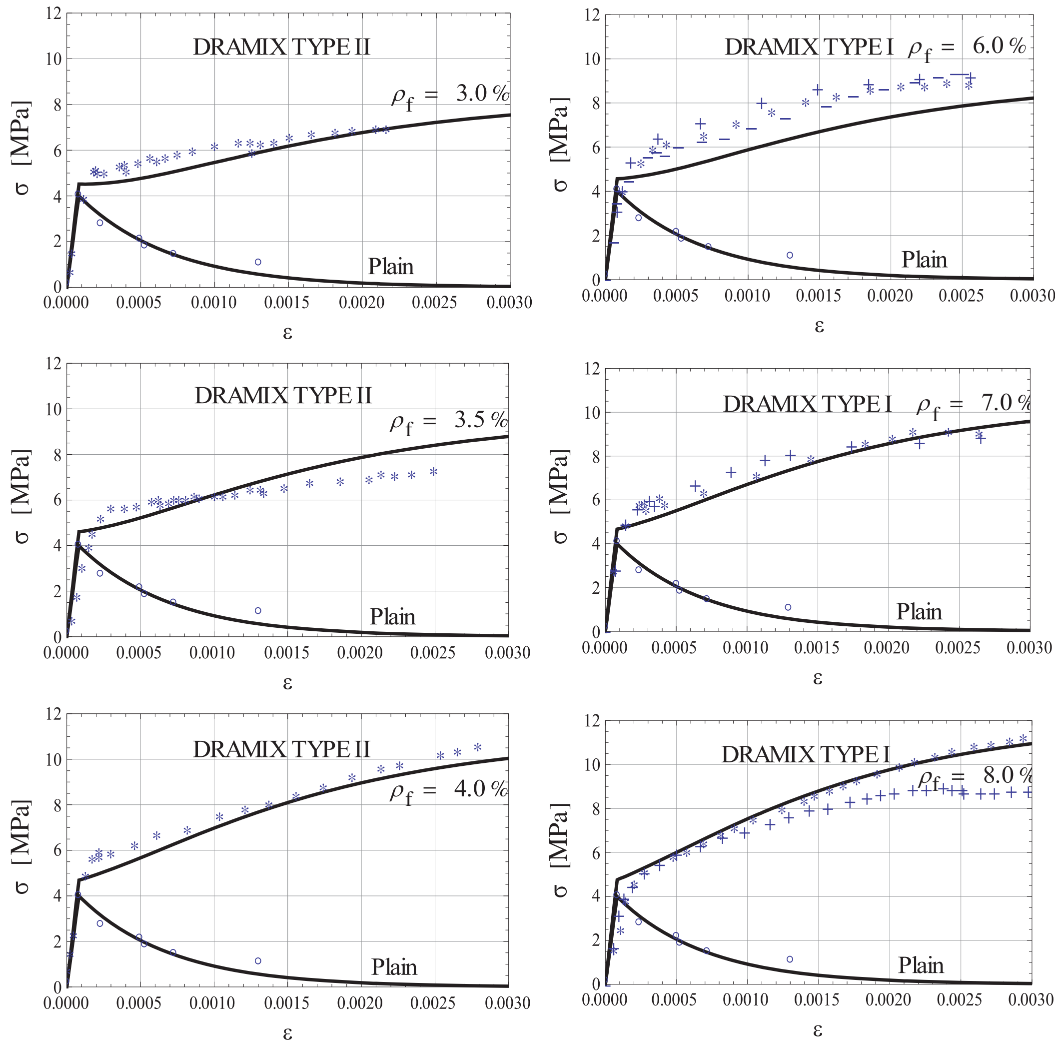

FIGURE 9 Comparison between numerical predictions and experimental results (dotted curves) by Li and Li[55] of SFRCs with Dramix type I and II.

- ○ Comparing numerical predictions and experimental results by Soltanzadeh et al.,[57] in terms of Shear load versus Lateral displacement curves in Section 5.3.2, with the aim to verify the predictive capacity of the dowel mechanism.
- ○ Analyzing the localized failure indicator in Section 5.3.3, to determine critical failure directions under shear loads.
- Uniaxial compression tests in Section 5.4. As largely accepted in the scientific literature, no significant difference can be observed in terms of strength and pre-peak behavior of SFRCs compared to plane concrete (see a. o.[12,58]). For this reason, the onset of localized failure in the plane concrete is evaluated. The advantages of the elliptical CAP inclusion in the yield function by analyzing the localized failure indicator is demonstrated.
- Triaxial compression tests in Section 5.5. The ductility increase for confined compression states, as demonstrated by the experimental tests by Chern et al.,[59] is numerically verified for variable fiber reinforcement percentages.

5.1 | Tensile tests: Comparison against experimental data

The regarded experimental campaign for SFRC in tension by Li and Li[55] have been performed on prismatic specimens with the dimensions $500 \times 100 \times 20$ mm^3, containing two fiber types, namely Dramix type I and II, whose fundamental characteristics as density, diameter d_f, length l_f, steel yield stress σ_y^s and elastic modulus E^s are given in Table 2. The material properties and model parameters adjusted according to the experimental

17517648, 0, Downloaded from https://onlinelibrary.wiley.com/doi/10.1002/suco.202300875 by Antonio Caggiano - University Degli Studi Di , Wiley Online Library on [22/12/2024]. See the Terms and Conditions (https://onlinelibrary.wiley.com/terms-and-conditions) on Wiley Online Library for rules of use; OA articles are governed by the applicable Creative Commons License

17517648, 0, Downloaded from https://onlinelibrary.wiley.com/doi/10.1002/suco.202300875 by Antonio Caggiano - University Degli Studi Di , Wiley Online Library on [22/12/2024]. See the Terms and Conditions (https://onlinelibrary.wiley.com/terms-and-conditions) on Wiley Online Library for rules of use; OA articles are governed by the applicable Creative Commons License

TABLE 3 Characterization of material properties and model parameters.

Tests	Tensile Li and Li[55]	Shear Soltanzadeh et al.[57]	Compression Chern et al.[59]
Concrete properties			
Elasticity modulus—E [GPa]	39.5	36	20
Poisson coefficient—ν	0.2	0.2	0.2
Bulk modulus—K [GPa]	21.9	20.0	11.1
Shear modulus—G [GPa]	16.45	15.0	8.3
Compressive strength—f'_c [MPa]	35.0	67.84	20.65
Tensile strength—χ_0^{mic} [MPa]	3.5	6.7	2.0
Initial cohesion—c_0^{mic} [MPa]	7.0	12.0	4.0
Internal friction—$\tan(\phi_0^{mic})$	0.6	0.6	0.6
Fract. energy mode I—G_f^{I} [N/mm]	0.12	0.16	0.09
Fract. energy mode II—G_f^{IIa} [N/mm]	1.2	1.6	0.9
Steel fibers properties			
Elasticity modulus—E^s [GPa]	200.0	200.0	200.0
Yield stress—σ_y^s [MPa]	1200.0	1100.0	1100.0
Fiber–concrete interfaces properties			
Equivalent elasticity modulus—E^f [GPa]	200.0	200.0	200.0
Equivalent yield stress—σ_y^f [MPa]	216.0	198.0	180.0
Equivalent shear modulus—G^f [GPa]	15.0	15.0	15.0
Equivalent shear strength—τ_y^s [MPa]	332.0	441.70	330.0
Hardening/softening modules—$H_N^f = H_T^f$	0.0	0.0	0.0
Model parameters			
α_χ [N/mm]	−0.15	−0.15	−0.15
l_{cs}^{I} [mm]	24	24	13
l_{cs}^{IIa} [mm]	24	24	13

data are summarized in the first column of Table 3.

Numerical predictions carried out in both plain concrete and SFRC with uniform distribution of fibers for analyzing tensile test cases, are presented in this section. The comparisons between model predictions and the cited experimental data in terms of Stress–Strain diagrams are reported in Figure 9.

The response for SFRCs with steel Dramix type II, characterized by fiber contents ranging between 3.0% and 4.0%, is given in the left side of Figure 9; while on the right, the corresponding to Dramix type I, with fiber contents of 6.0%, 7.0%, and 8.0%, are reported. In all cases, very good agreement is obtained. The model predicts in a very realistic mode the mechanical response of the analyzed SFRC specimens.

It is worth highlighting that all the other numerical curves have been obtained by just changing the fiber contents (ρ_f) and/or fiber types (e.g., l_f) according to the properties given by the experimental report. This aspect is the key advantage of modeling the fiber effects in an explicit way: it gives the possibility of obtaining the overall macroscopic Stress–Strain response by just changing the fiber type and geometry.

5.2 | Comparison with the zero-thickness interface model under uniaxial tension

This section addresses the effect of comparing the mechanical response of FRCC simulated by the continuous microplane-based model developed in this work with the zero-thickness interface discontinuous formulation given by the authors in Caggiano et al.[15]

The simulations of 1.0 cm-edge cubic samples, as proposed in Figures 8a and 10 and are analyzed. Variable interfaces and microplanes number are considered,

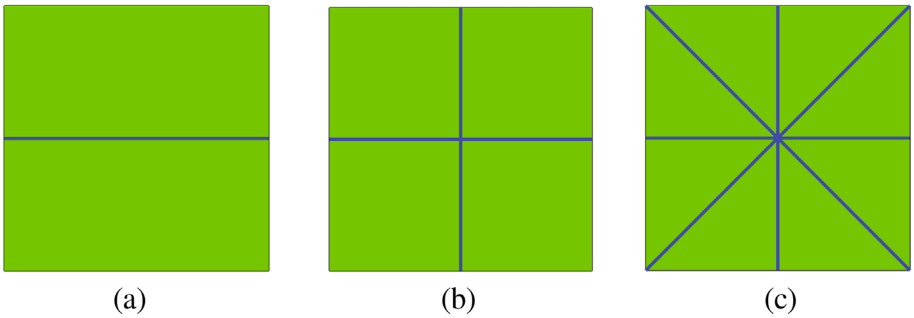

FIGURE 10 FE discretization including the cases of: (a) one, (b) four, and (c) eight interfaces.

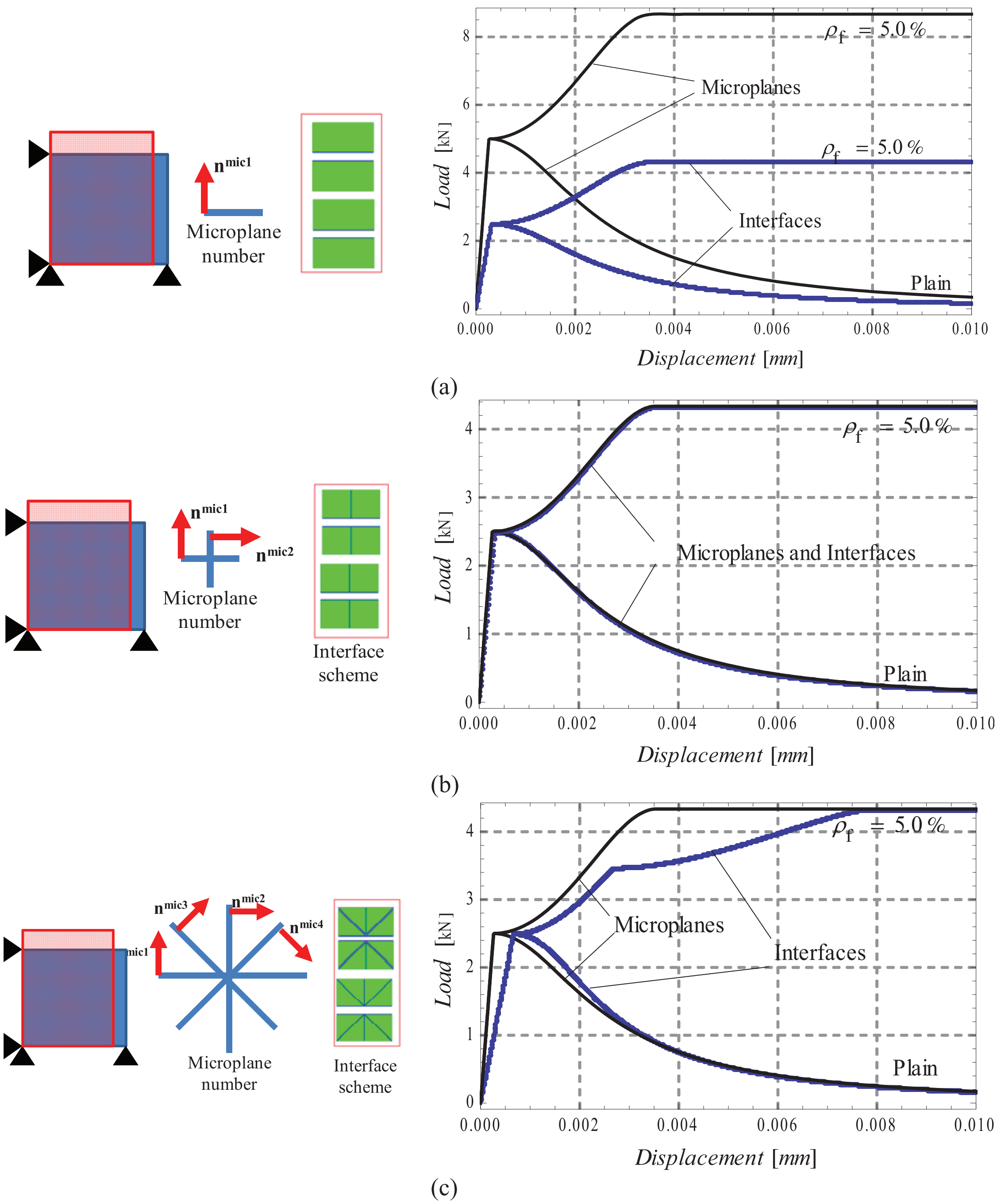

FIGURE 11 Interface-based simulations versus microplane ones under tensile load.

17517648, 0, Downloaded from https://onlinelibrary.wiley.com/doi/10.1002/suco.202300875 by Antonio Caggiano - University Degli Studi Di , Wiley Online Library on [22/12/2024]. See the Terms and Conditions (https://onlinelibrary.wiley.com/terms-and-conditions) on Wiley Online Library for rules of use; OA articles are governed by the applicable Creative Commons License

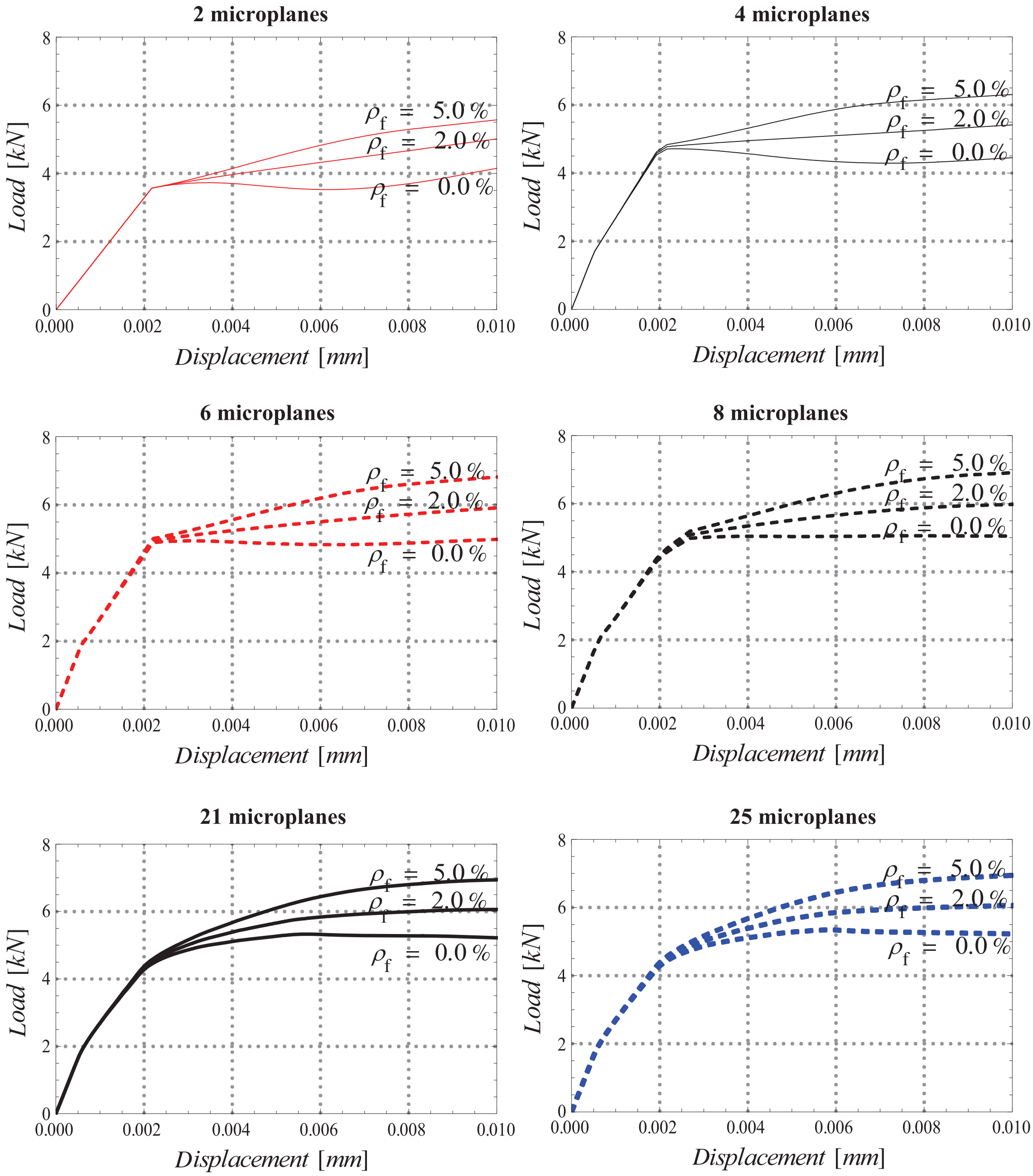

FIGURE 12 Lateral shear load versus Displacement predictions with microplanes number varying from 2 to 25 and variable fiber percentages.

taking into account the plane formulation by Park and Kim [56] for the latter. Plane stress hypothesis and displacement-based control are assumed. Then, two material types are considered: (i) plain concrete and (ii) SFRC with fiber percentage $\rho_f = 5.0\%$.

To compare the response of the two mentioned approaches in terms of Load versus Displacement laws (result of the structural response achieved by employing the discontinuous-based formulation with the discretizations of Figure 10), the load is now measured by multiplying the vertical stress by the cross section of the specimen (1×1 cm^2 in case of plane stress), while the vertical displacement is intended as the tensile strain which multiplies the specimen height (1 cm).

As schematized on the left of Figure 11, three interfaces/microplanes distributions are reported:

- 1 horizontal interface versus 1 microplane over the unit hemisphere,

17517648, 0, Downloaded from https://onlinelibrary.wiley.com/doi/10.1002/suco.202300875 by Antonio Caggiano - University Degli Studi Di , Wiley Online Library on [22/12/2024]. See the Terms and Conditions (https://onlinelibrary.wiley.com/terms-and-conditions) on Wiley Online Library for rules of use; OA articles are governed by the applicable Creative Commons License

- 2 horizontal interfaces versus 2 microplanes over the unit hemisphere and
- 4 horizontal interfaces versus 4 microplanes over the unit hemisphere.

The comparison of the resulting curves is shown on the right. Based on such simulations, it can be observed that at least 2 microplanes over the unit hemisphere must be considered to achieve an acceptable accuracy of the numerical integration in case of pure tensile stress. The numerical responses of the tests involving 4 horizontal interfaces and 4 microplanes highlight that greater number of interfaces is responsible of a less ductile structural response in post-cracking regime.

As mentioned in Section 2, the macroscopic stress tensor can be theoretically evaluated by imposing the equilibrium between micro- and macroscopic scales, according Equation (9). However, its integration is transformed into a summation, which is characterized by a finite number of considered orientations (equal to the adopted discretizing microplanes), getting Equation (10).

5.3 | Shear tests

Numerical predictions of shear tests have been carried out for three purposes:

- To verify the accuracy of the numerical response with respect to variable microplanes number, finding the minimum that gives the exact solution.
- To evaluate the contribution of the dowel mechanism of fibers crossing cracks on the overall behavior, comparing numerical predictions and experimental results in terms of Shear load versus Lateral displacement curves.
- In addition, localized failure indicator performance has been analyzed to evaluate the orientation of critical directions for discontinuous bifurcation.

5.3.1 | Accuracy of the numerical response

The accuracy of the numerical response, based on the number of the considered microplanes at the unit hemisphere, is investigated in the case of simple shear test. For this purpose, 2, 4, 6, 8, 21, and 25 microplanes (on the unit hemisphere) are considered. The results can be found in Figures 12 and 13, where the Lateral load versus Displacement curves have been plotted. Particularly, Figure 12 emphasizes the comparative response of three kinds of concretes:

- Plain concrete,

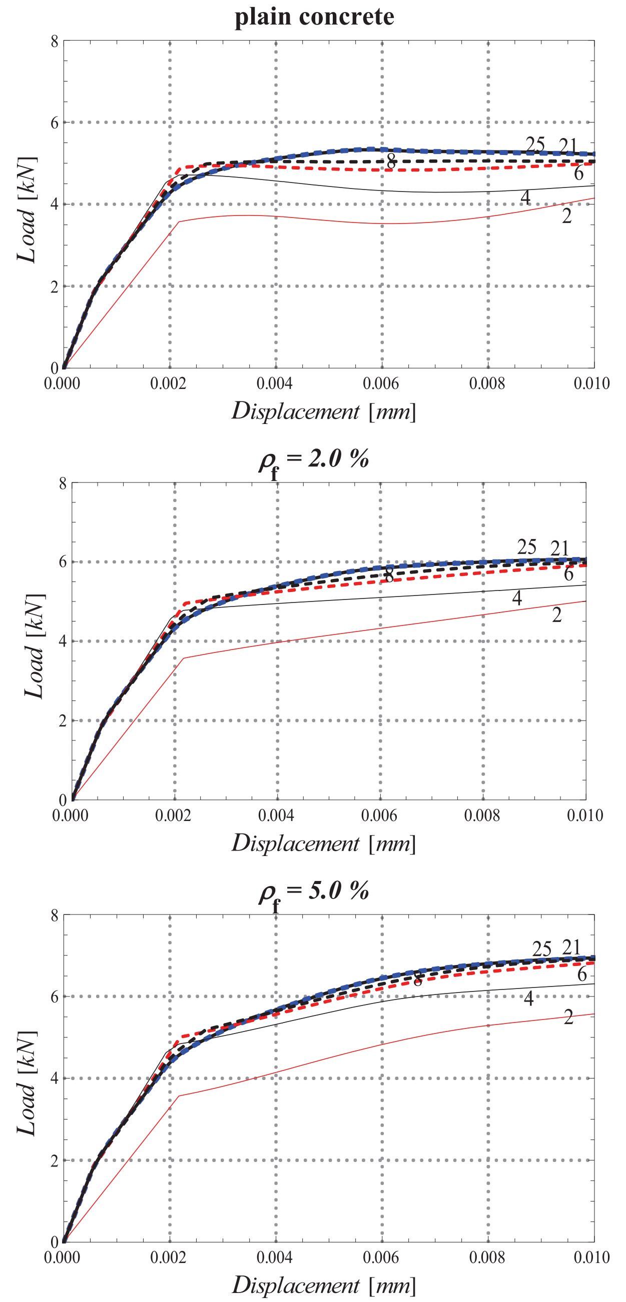

FIGURE 13 Lateral shear load versus Displacement comparisons with variable microplanes number and fiber contents.

- SFRC with fiber contents of 2.0%, and
- SFRC with 5.0% of steel fibers.

This figure clearly highlights the phenomenological effect of fibers when are added on a cementitious matrix. Fiber inclusions mainly enhance the mechanical property of SFRC in terms of both shear strength and ductility.

Then, Figure 13 highlights the difference in responses when a variable number of microplanes are considered. In each subfigure, the responses for a variable number of microplanes have been superimposed. It can be stated

17517648, 0, Downloaded from https://onlinelibrary.wiley.com/doi/10.1002/suco.202300875 by Antonio Caggiano - University Degli Studi Di , Wiley Online Library on [22/12/2024]. See the Terms and Conditions (https://onlinelibrary.wiley.com/terms-and-conditions) on Wiley Online Library for rules of use; OA articles are governed by the applicable Creative Commons License

that an acceptable accuracy involves at least 21 microplanes of integration, as also demonstrated in the work by.[60] A poor approximation, which takes place for a lower number, can be observed around the peak strength and in the post-peak regime.

5.3.2 | Comparison against experimental data

In this section, experimental results of the direct shear test by Soltanzadeh et al.,[57] are considered. Specially designed double shear specimens, that is, rectangular specimens of $150 \times 146\ \text{mm}^2$ cross-section and 47 mm thick, with two notches of 25 mm depth and 5 mm width at the top and bottom edges to localize the shear crack along the predefined shear planes, have been used. High Performance Fiber Reinforced Concrete (HPFRC) with 4.0% of steel fibers reinforcement has been employed, characterized by the material properties and model parameters highlighted in the second column of Table 3.

A total of 42 microplanes with random distribution of fibers has been considered. Numerical predictions compared against experimental results in terms of Shear load versus Lateral displacement curves are shown in Figure 14, where a good approximation can be verified. By comparing the response of plane and reinforced concrete, the improvement of the composite mechanical behavior in terms of toughness and peak strength can be captured by the proposed microplane-based constitutive theory.

5.3.3 | Onset of strain localization

With the aim to determine critical failure directions under shear loads, numerical localization analysis at peak stress state of the shear test has been performed.

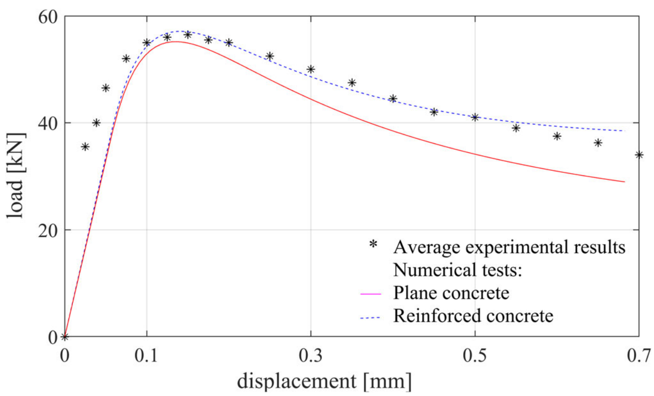

FIGURE 14 Predictions of Shear load versus Lateral displacement of the shear test by Soltanzadeh et al.[57] Fibers content $\rho_f = 4.0\%$.

Results of the normalized localized failure indicator $[\det(\boldsymbol{Q}^{ep})/\det(\boldsymbol{Q}^{e})]$ are shown in Figure 15. The obtained critical failure directions are oriented at $\theta_{c1} = 45°$ and $\theta_{c2} = 135°$, in agreement with the experimental evidence. According to Soltanzadeh et al.,[57] during the loading process of the specimens, several small diagonal cracks developed along the ligaments of the double shear specimen.

5.4 | Uniaxial compression tests: Comparison against experimental data and discontinuous bifurcation analysis

The overall performance of the proposed constitutive model for the uniaxial compression case is verified by comparisons of the numerical results against the experimental predictions by Chern et al.,[59] in terms of Compressive stresses versus Strains curves (Figure 16). Considered material properties and model parameters are displayed in the third column of Table 3. Since the experiments were performed on cylindrical specimens of 58 mm in diameter and 108 mm in height, the numerical analyses were done under cylindrical stress conditions. Plain concrete and SFRC with 1.0% and 2.0% fiber content have been considered. Very good agreement can be appreciated for all three cases. Once again, the sensitivity to fiber reinforcement is demonstrated. With increasing percentages of fibers, the peak stress and strain increase as well as the concrete toughness.

From the analysis of discontinuous bifurcation through the localized failure condition of Section 4, arises an important advantage of the inclusion of the elliptical CAP as a complement of the hyperbolic yield function, in addition to the better mechanical response in case of high compression load states.

The performance of the normalized localization indicator $[\det(\boldsymbol{Q}^{ep})/\det(\boldsymbol{Q}^{e})]$ at peak stress states is evaluated regarding both, the yield function with and without CAP.

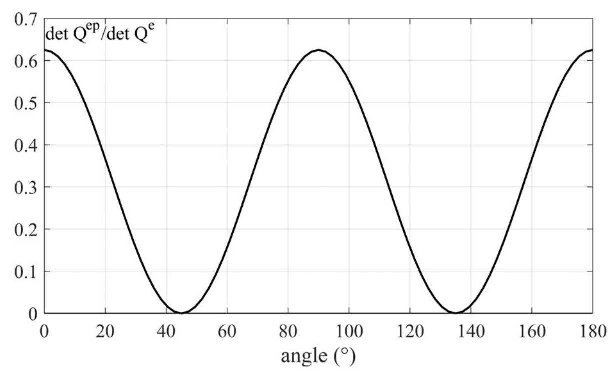

FIGURE 15 Numerical localization analysis with the microplane-based model at peak of the shear test.

17517648, 0, Downloaded from https://onlinelibrary.wiley.com/doi/10.1002/suco.202300875 by Antonio Caggiano - University Degli Studi Di , Wiley Online Library on [22/12/2024]. See the Terms and Conditions (https://onlinelibrary.wiley.com/terms-and-conditions) on Wiley Online Library for rules of use; OA articles are governed by the applicable Creative Commons License

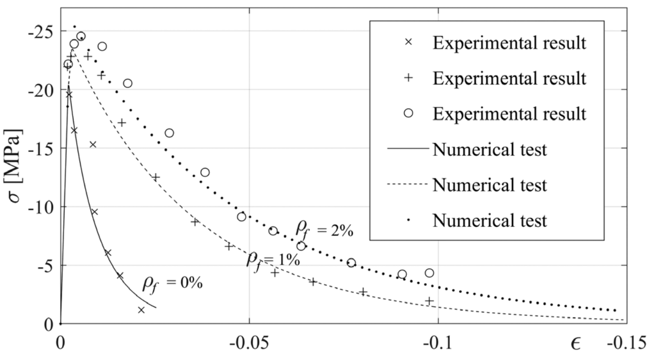

FIGURE 16 Comparisons between numerical predictions and experimental results of uniaxial compression tests by Chern et al.[59]

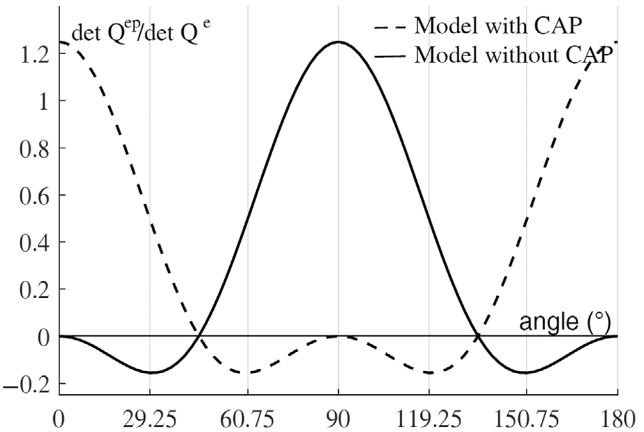

FIGURE 17 Numerical localization analysis with the microplane-based model at peak of the simple uniaxial compression test.

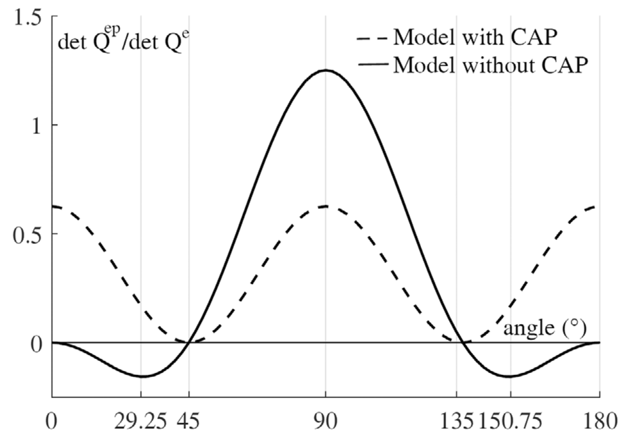

FIGURE 18 Numerical localization analysis with the microplane-based model at peak of confined compression test.

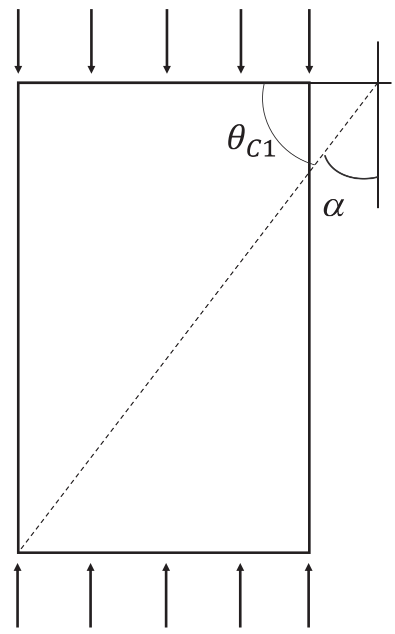

FIGURE 19 Onset of the strain localization of compressed concrete.

Both, failure modes, that is, localized or diffuse by means of negative or positive values, respectively, as well as critical directions are obtained.

First, regarding the uniaxial compression stress state corresponding to the vertex of the CAP in Figure 6, failure modes and critical directions are evaluated in Figure 17. Regarding the constitutive model with CAP, localization surfaces are characterized by their normal directions, oriented at $\theta_{c1} = 60.75°$ and $\theta_{c2} = 119.25°$ with respect to the principal directions, respectively. Whereas the constitutive model without CAP predicts localized or brittle failure modes with critical directions at $\theta_{c1} = 29.25°$ and $\theta_{c2} = 150.75°$. The influence of the increasing confining pressure in the evolution of failure modes is shown in Figure 18, representing the peak stresses of the CAP. Regarding the constitutive model with elliptical CAP, normal directions of localization surfaces are oriented at $\theta_{c1} = 45°$ and $\theta_{c2} = 135°$ with respect to the principal directions. Whereas for a yield function without CAP, these surfaces are also given at $\theta_{c1} = 29.25°$ and $\theta_{c2} = 150.75°$, as in the previous case. It can be clearly observed that increasing confinement must lead to more stable or ductile failure modes, with variable critical directions, as is the case of the model with elliptical CAP.

Experimental measurements support these findings. Fujita et al.[61] experimentally determined that the angle between the sliding plane and the direction of the applied load in uniaxial compression (α, as illustrated in Figure 19), was 18°. Similarly, in the study by Sfer et al.,[62] α was measured as 16°. In contrast, Fantilli et al.[63] observed strain localization and diagonal cracks oriented to mostly 45° during triaxial compression tests. The present formulation demonstrates a similar tendency.

17517648, 0, Downloaded from https://onlinelibrary.wiley.com/doi/10.1002/suco.202300875 by Antonio Caggiano - University Degli Studi Di , Wiley Online Library on [22/12/2024]. See the Terms and Conditions (https://onlinelibrary.wiley.com/terms-and-conditions) on Wiley Online Library for rules of use; OA articles are governed by the applicable Creative Commons License

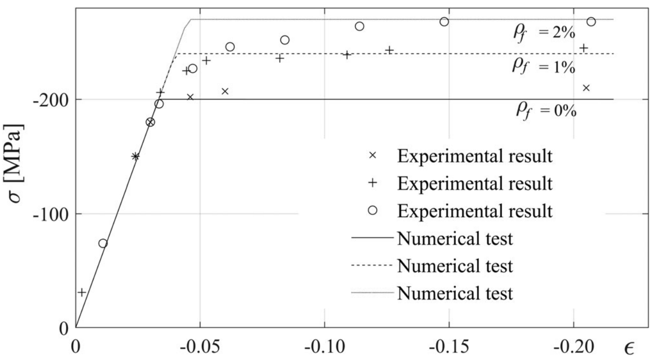

FIGURE 20 Comparisons between numerical predictions and experimental results of triaxial compression tests by Chern et al.[59]

5.5 | Triaxial compression tests

The results of the confined compression experimental campaign by Chern et al.,[59] performed on concrete cylinders of $100 \times 200\ \text{mm}^2$ with variable content of fibers, that is, $\rho_f = 0.0\%, 1.0\%$, and 2.0%, with a lateral confinement of 70 MPa, have been considered. According to Figure 20, where they are compared against numerical predictions, the ductility of SFRC increases with the percentage of fiber reinforcement.

6 | CONCLUSIONS

This work presents a microplane-based elasto-plasticity approach aimed at simulating the failure behavior of Fiber Reinforced Cementitious Composites (FRCC) at the material level. The constitutive model incorporates the well-known Mixture Theory to simulate the combined bridging interactions of fibers in concrete cracks, which are associated with bond–slip and dowel mechanisms. At the microplane level, the behavior of the cementitious matrix is described by a hyperbolic maximum strength criterion with an elliptical CAP surface. Differentiated plastic flow rules and fracture energy-based softening laws are applied. Rankine-type functions are adopted to describe the elasto-plastic yield of fibers. The main contributions of the proposed model that differentiate it from existing ones are: (i) normal and tangential stresses at microplane level arise from thermodynamic principles, (ii) the yield function for the concrete matrix defines in a single mathematical expression the entire spectrum of possible stress states, (iii) the inclusion of the elliptic CAP in the yield function limits the high confinement zone, and (iv) the inclusion of the dowel effect of fibers is added to the bond-slip bridging-mechanism. Numerical simulations demonstrate that the proposed constitutive model captures the fundamental behaviors of FRCC. Excellent agreement was achieved between the numerical results and experimental data available in the scientific literature, particularly in terms of peak strength and post-cracking toughness for tensile, compression and shear tests. The numerical analyses of localization in the high confinement regime of the proposed constitutive model with CAP demonstrate an increase in the positive definition of the localization tensor, as well as an increase in the related critical localization angle with the applied confinement. The microplane-based constitutive formulation for FRCC is capable of reproducing the transition of the critical directions from uniaxial compressive to combined shear/compression states.

ACKNOWLEDGMENTS

The authors acknowledge the partial financial support for this work by CIUNT (Research Council of the University of Tucuman, Argentina) through the Grant no. E-754. Open access publishing facilitated by Universita degli Studi di Genova, as part of the Wiley - CRUI-CARE agreement.

DATA AVAILABILITY STATEMENT

The data that support the findings of this study are available from the corresponding author upon reasonable request.

ORCID

Antonio Caggiano https://orcid.org/0000-0003-1027-2520
Sonia M. Vrech https://orcid.org/0000-0002-5039-754X

REFERENCES

1. Signorini C, Nobili A. Durability of fibre-reinforced cementitious composites (FRCC) including recycled synthetic fibres and rubber aggregates. Appl Eng Sci. 2021;9:100077.
2. Truong VD, Noh HW, Kim DJ. Effects of adding short fibers on impact resistance of glass textile reinforced cementitious composites under direct tension. Construct Build Mater. 2023;379:131220.
3. Şanal N, Özyurt I, Hosseini A. Characterization of hardened state behavior of self compacting fiber-reinforced cementitious composites (SC-FRCC's) with different beam sizes and fiber types. Compos Part B Eng. 2016;105:30–45.
4. Kim MK, Kim DJ. Electromechanical response of strain-hardening fiber-reinforced cementitious composites (SH-FRCCs) under direct tension: A review. Sens Actuators A Phys. 2023;349:114096.
5. Hao Y, Cheng L, Hao H, Shahin MA. Enhancing fiber/matrix bonding in polypropylene fiber reinforced cementitious composites by microbially induced calcite precipitation pre-treatment. Cem Concr Composites. 2018;88:1–70.
6. Feng J, Yang F, Qian S. Improving the bond between polypropylene fiber and cement matrix by nano calcium carbonate modification. Construct Build Mater. 2020;269:121249.

17517648, 0, Downloaded from https://onlinelibrary.wiley.com/doi/10.1002/suco.202300875 by Antonio Caggiano - University Degli Studi Di , Wiley Online Library on [22/12/2024]. See the Terms and Conditions (https://onlinelibrary.wiley.com/terms-and-conditions) on Wiley Online Library for rules of use; OA articles are governed by the applicable Creative Commons License

7. Bediwy A, Mahmoud K, El-Salakawy E. Structural behavior of frcc layered deep beams reinforced with GFRP headed-end bars. Eng Struct. 2021;243:112648.
8. Wu B, Liu Y, Feng P, Qiu J. Cracking can make concrete stronger—the coupled effect of matrix cracking and SiO2-enhanced fiber/matrix interface healing on the tensile strength of FRCC. Cem Concr Composites. 2023;138:105011.
9. Cai J, Sheng Z, Wang X, Fang Y, Pan J. Effect of reinforcement configurations on the flexural behaviors of 3D printed fiber reinforced cementitious composite FRCC beams. J Build Eng. 2022;46:103773.
10. Naaman A, Reinhardt H. Proposed classification of HPFRC composites based on their tensile response. Mater Struct. 2006; 39:547–55.
11. di Prisco M, Plizzari G, Vandewalle L. Fibre reinforced concrete: new design perspectives. Mater Struct. 2009;42:1261–81.
12. Fantilli AP, Mihashi H, Vallini P. Multiple cracking and strain hardening in fiber-reinforced concrete under uniaxial tension. Cem Concr Res. 2009;39:1217–29.
13. Prasad M, Krishnamoorthy C. Computational model for discrete crack growth in plain and reinforced concrete. Comput Methods Appl Mech Eng. 2002;191:2699–725.
14. Etse G, Caggiano A, Vrech S. Multiscale failure analysis of fiber reinforced concrete based on a discrete crack model. Int J Fract. 2012;178:131–46.
15. Caggiano A, Vrech S, Etse G. Discontinuous bifurcation of FRCC with zero-thickness interface modeling. Mech Res Commun. 2023;129:104088.
16. Bi J, Huo L, Zhao Y, Qiao H. Modified the smeared crack constitutive model of fiber reinforced concrete under uniaxial loading. Construct Build Mater. 2020;250:118916.
17. Freddi F, Royer-Carfagni G. Regularized variational theories of fracture: a unified approach. J Mech Phys Solids. 2010;58: 1154–74.
18. Cervera M, Wu J-Y. On the conformity of strong, regularized, embedded and smeared discontinuity approaches for the modeling of localized failure in solids. Int J Solids Struct. 2015; 71:19–38.
19. Wosatko A, Genikomsou A, Pamin J, Polak MA, Winnicki A. Examination of two regularized damage-plasticity models for concrete with regard to crack closing. Eng Fract Mech. 2018; 194:190–211.
20. Bažant Z, Oh B. Crack band theory for fracture of concrete. RILEM—Mater Structs. 1983;93:155–77.
21. Carol I, Jirasek M, Bažant Z. A thermodynamically consistent approach to microplane theory. Part I. Free energy and consistent microplane stresses. Int J Solids Struct. 2001;38:2921–31.
22. Kuhl E, Steinmann P, Carol I. A thermodynamically consistent approach to microplane theory. Part II. Dissipation and inelastic constitutive modeling. Int J Solids Struct. 2001;38:2933–52.
23. L. Huang, J. Li, N. Tue, Numerical aspects of microplane constitutive models for concrete, App Math Model 38 (2017) 530–48.
24. Indriyantho B, Zreid I, Kaliske M. A nonlocal softening plasticity based on microplane theory for concrete at finite strains. Comput Struct. 2020;241:106333.
25. Kong L, Xie H, Li C. Coupled microplane and micromechanics model for describing the damage and plasticity evolution of quasi-brittle material. Int J Plast. 2023;162:103549.
26. Ferhun C, Caner F, Bažant Z, Wendner R. Microplane model M7f for fiber reinforced concrete. Eng Fract Mech. 2013;105: 41–57.
27. Vrech S, Etse G, Caggiano A. Thermodynamically consistent elasto-plastic microplane formulation for fiber reinforced concrete. Int J Solids Structures. 2016;81:337–49.
28. Xue J, Kirane K. Cylindrical microplane model for compressive kink band failures and combined friction/inelasticity in fiber composites I: formulation. Composite Struct. 2022;289:11538.
29. Truesdell C, Toupin R. The classical field theories. In: Handbuch der Physik. Berlin, Germany: Springer; 1960. p. 226–858.
30. Ortiz M, Popov EP. Plain concrete as a composite material. Mech Mater. 1982;1:139–50.
31. Oller S, Oñate E, Miquel J, Botello S. A plastic damage constitutive model for composite materials. Int J Solids Struct. 1996; 33:2501–18.
32. Rastellini F, Oller S, Salomón O, Oñate E. Composite materials non-linear modelling for long fibre-reinforced laminates. Continuum basis, computational aspects and validations. Comput Struct. 2008;861:879–96.
33. Oliver J, Linero D, Huespe A, Manzoli O. Two-dimensional modeling of material failure in reinforced concrete by means of a continuum strong discontinuity approach. Comput Methods Appl Mech Eng. 2008;197:332–48.
34. Vrech S, Etse G, Meschke G, Caggiano A, Martinelli E. Meso- and macroscopic models for fiber-reinforced concrete. In: Bicanic N, de Borst R, Mang H, Meschke G, editors. Computational modelling of concrete structures. Rohrmoos/Schladming, Austria: CRC Press; 2010.
35. Coleman B, Noll W. The thermodynamics of elastic materials with heat conduction and viscosity. Arch Rational Mech Anal. 1963;13:167–78.
36. Coleman B, Gurtin M. Thermodynamics with internal state variables. J Chem Phys. 1967;47:597–613.
37. Bažant Z, Oh B. Microplane model for progressive fracture of concrete and rock. J Eng Mech ASCE. 1985;111:559–82.
38. Carol I, Prat P, Lopez C. Normal/shear cracking model: applications to discrete crack analysis. J Eng Mech ASCE. 1997;123: 765–73.
39. Krenchel H. Fiber spacing and specific fiber surface. In: Neville A, editor. Fibre reinforced cement and concrete. UK: The Construction Press; 1975.
40. Dupont D, Vandewalle L. Distribution of steel fibres in rectangular sections. Cem Concr Composites. 2005;27:391–8.
41. Soroushian P, Lee C. Distribution and orientation of fibers in steel fiber reinforced concrete. Cem Concr Composites. 1990; 87:433–9.
42. Leukart M. Kombinierte Anisotrope Schädigung und Plastizität bei kohaesiven Reibungsmaterialien, PhD thesis, Institut fur Baustatik der Universitat Stuttgart. 2005.
43. Kanatani KI. Distribution of directional data and fabric tensors. Int J Eng Sci. 1984;22:149–64.
44. Lubarda VA, Krajcinovic D. Damage tensors and the crack density distribution. Int J Solids Struct. 1993;30:2859–77.
45. Caggiano A. Meso-mechanical analysis of steel fiber reinforced cementitious composites, PhD thesis, Università degli Studi di Salerno-Universidad Nacional de Tucuman. 2011.
46. Atkinson R, Amadei B, Saeb S, Sture S. Response of masonry bed joints in direct shear. J Struct Eng. 1989;115:2276–96.

17517648, 0, Downloaded from https://onlinelibrary.wiley.com/doi/10.1002/suco.202300875 by Antonio Caggiano - University Degli Studi Di , Wiley Online Library on [22/12/2024]. See the Terms and Conditions (https://onlinelibrary.wiley.com/terms-and-conditions) on Wiley Online Library for rules of use; OA articles are governed by the applicable Creative Commons License

47. Pande G, Beer G, Williams J. Numerical methods in rock mechanics. New York: John Wiley & Sons Inc; 1990.
48. Martínez A, Liaudat J, López CM, Carol I. 3D zero-thickness interface model for fracture of cement-based materials with chemical degradation. Int J Solids Struct. 2022;238:111379.
49. Lorefice R, Etse G, Carol I. Viscoplastic approach for rate-dependent failure analysis of concrete joints and interfaces. Int J Solids Struct. 2008;45:2686–705.
50. Caballero A, Willam K, Carol I. Consistent tangent formulation for 3D interface modeling of cracking/fracture in quasi-brittle materials. Comput Methods Appl Mech Eng. 2008;197:2804–22.
51. El-Ariss B. Behavior of beams with dowel action. Eng Struct. 2007;29:899–903.
52. Dei Poli S, Di Prisco M, Gambarova P. Shear response, deformations, and subgrade stiffness of a dowel bar embedded in concrete. ACI Struct J. 1992;89:665–75.
53. Soroushian P, Obaseki K, Rojas M. Bearing strength and stiffness of concrete under reinforcing bars. ACI Mater J. 1987;84:179–84.
54. Dulacska H. Dowel action of reinforcement crossing cracks in concrete. ACI Struct J. 1972;69:754–7.
55. Li F, Li Z. Continuum damage mechanics based modeling of fiber reinforced concrete in tension. Int J Solids Struct. 2001;38:777–93.
56. Park H, Kim H. Microplane model for reinforced-concrete planar members in tension-compression. J Struct Eng. 2004;129:337–45.
57. Soltanzadeh F, Barros J, Santos R. High performance fiber reinforced concrete for the shear reinforcement: experimental and numerical research. Construct Build Mater. 2015;77:94–109.
58. Nataraja M, Dhang N, Gupta A. Stress-strain curves for steel-fiber reinforced concrete under compression. Cem Concr Composites. 1999;21:383–90.
59. Chern J, Yang H, Chen H. Behavior of steel fiber-reinforced concrete in multiaxial loading. ACI Mater J. 1992;89:32–40.
60. Bažant Z, Oh B. Efficient numerical integration on the surface of a sphere. Int J Solids Struct. 1986;66:37–49.
61. Fujita Y, Ishimaru R, Hanai S, Suenaga Y. Study on internal friction angle and tensile strength of plain concrete, proceedings of fracture mechanics of concrete structures FRAMCOS 3. Freiburg, Germany: Aedificatio Publishers; 1998. p. 325–43.
62. Sfer D, Carol I, Gettu R, Etse G. Experimental study of the triaxial behavior of concrete. ASCE J Eng Mech. 2002;12:156–63.
63. Fantilli A, Vallini P, Chiaia B. Ductility of fiber-reinforced self-consolidating concrete under multi-axial compression. Cem Concr Composites. 2011;33:520–7.

AUTHOR BIOGRAPHIES

Antonio Caggiano[a], DICCA, Department. of Civil, Chemical and Environmental Engineering, University of Genova, Via Montallegro 1, Genova 16145, Italy. Email: antonio.caggiano@unige.it

Sonia M. Vrech, CONICET, National Scientific and Technical Research Council, Buenos Aires, Argentina. Email: svrech@herrera.unt.edu.ar

Guillermo Etse[b], CEMNCI, Center for Numerical and Computational Methods in Engineering, Faculty of Exact Sciences and Engineering, National University of Tucuman, Av. Independencia 1800, Tucumán 4000, Argentina. Email: getse@herrera.unt.edu.ar

How to cite this article: Caggiano A, Vrech SM, Etse G. Hyperbolic/elliptic-CAP formulation for FRCC based on microplane constitutive theory. Structural Concrete. 2024. https://doi.org/10.1002/suco.202300875

17517648, 0, Downloaded from https://onlinelibrary.wiley.com/doi/10.1002/suco.202300875 by Antonio Caggiano - University Degli Studi Di , Wiley Online Library on [22/12/2024]. See the Terms and Conditions (https://onlinelibrary.wiley.com/terms-and-conditions) on Wiley Online Library for rules of use; OA articles are governed by the applicable Creative Commons License

APPENDIX A: Localized failure indicator

In the framework of the SCA, localized failure modes involves the occurrence of weak discontinuities in the strains rate field while the velocity displacements rate field is assumed to remain continuous. According to the Maxwell's compatibility theorem,[29] the jump in the rate of the displacement gradient may be expressed in terms of a scalar-valued jump amplitude $\dot{\gamma}$, the unit jump vector $\boldsymbol{M}$ and the unit normal vector to the discontinuity surface $\boldsymbol{N}_{\mathrm{d}}$, as

$$[[\nabla \dot{\boldsymbol{u}}]] = \dot{\gamma} \boldsymbol{M} \bigotimes \boldsymbol{N}_{\mathrm{d}}. \tag{A.1}$$

Consequently, the strain rate discontinuity is defined by the symmetrized dyadic of the unit vectors $\boldsymbol{M}$ and $\boldsymbol{N}_{\mathrm{d}}$, by

$$[[\dot{\boldsymbol{\varepsilon}}]] = [[\nabla^{\mathrm{s}} \dot{u}]] = \frac{1}{2} \dot{\gamma} \left(\boldsymbol{M} \bigotimes \boldsymbol{N}_{\mathrm{d}} + \boldsymbol{N}_{\mathrm{d}} \bigotimes \boldsymbol{M} \right) = \dot{\gamma} \left(\boldsymbol{M} \bigotimes \boldsymbol{N}_{\mathrm{d}} \right)^{\mathrm{s}}. \tag{A.2}$$

In elasto-plasticity, regarding the tangent constitutive relation $\boldsymbol{\sigma} = \boldsymbol{E}^{\mathrm{ep}} : \dot{\boldsymbol{\varepsilon}}$, the balance of the linear momentum across the discontinuity surface leads to the localization condition

$$\dot{\boldsymbol{t}} = \boldsymbol{N}_{\mathrm{d}} \cdot [[\boldsymbol{\sigma}]] = \boldsymbol{N}_{\mathrm{d}} \cdot \boldsymbol{E}^{\mathrm{ep}} : [[\dot{\boldsymbol{\varepsilon}}]] = \dot{\gamma} \boldsymbol{N}_{\mathrm{d}} \cdot \boldsymbol{E}^{\mathrm{ep}} : \left(\boldsymbol{M} \bigotimes \boldsymbol{N}_{\mathrm{d}} \right)^{\mathrm{s}} = \dot{\gamma} \boldsymbol{N}_{\mathrm{d}} \cdot \boldsymbol{E}^{\mathrm{ep}} : \left(\boldsymbol{M} \bigotimes \boldsymbol{N}_{\mathrm{d}} \right)^{\mathrm{s}} = \dot{\gamma} \boldsymbol{Q}^{\mathrm{ep}} \cdot \boldsymbol{M} \doteq \boldsymbol{0}, \tag{A.3}$$

being $\boldsymbol{Q}^{\mathrm{ep}}$ the localization (acoustic) tensor, computed as

$$\boldsymbol{Q}^{\mathrm{ep}} = \boldsymbol{N}_{\mathrm{d}} \cdot \boldsymbol{E}^{\mathrm{ep}} \cdot \boldsymbol{N}_{\mathrm{d}} = \boldsymbol{Q} - \frac{1}{h_{\mathrm{p}}} \boldsymbol{a}_m \bigotimes \boldsymbol{a}_n \tag{A.4}$$

with

$$\boldsymbol{a}_m = \boldsymbol{N}_{\mathrm{d}} \cdot \boldsymbol{E} : \frac{\partial Q}{\partial \boldsymbol{\sigma}}, \quad \boldsymbol{a}_n = \frac{\partial F}{\partial \boldsymbol{\sigma}} : \boldsymbol{E} \cdot \boldsymbol{N}_{\mathrm{d}}, \tag{A.5}$$

and

$$h_{\mathrm{p}} = H + \frac{\partial F}{\partial \boldsymbol{\sigma}} : \boldsymbol{E} : \frac{\partial Q}{\partial \boldsymbol{\sigma}}. \tag{A.6}$$

Discontinuous bifurcation initiates when the localization tensor exhibits a singularity, that is, $\det(\boldsymbol{Q}^{\mathrm{ep}}) = 0$, for some critical directions of $\boldsymbol{M}$ and $\boldsymbol{N}_{\mathrm{d}}$. In Eqs. A.2 and A.3, the term "s" denotes the symmetry operation.

17517648, 0, Downloaded from https://onlinelibrary.wiley.com/doi/10.1002/suco.202300875 by Antonio Caggiano - University Degli Studi Di , Wiley Online Library on [22/12/2024]. See the Terms and Conditions (https://onlinelibrary.wiley.com/terms-and-conditions) on Wiley Online Library for rules of use; OA articles are governed by the applicable Creative Commons License